

Multi-sample SPIM image acquisition, processing and analysis of vascular growth in zebrafish

Stephan Daetwyler^{1,2,3}, Ulrik Günther^{1,3,4}, Carl D. Modes^{1,3}, Kyle Harrington^{5,*} and Jan Huiskens^{1,6,7,*}

ABSTRACT

To quantitatively understand biological processes that occur over many hours or days, it is desirable to image multiple samples simultaneously, and automatically process and analyse the resulting datasets. Here, we present a complete multi-sample preparation, imaging, processing and analysis workflow to determine the development of the vascular volume in zebrafish. Up to five live embryos were mounted and imaged simultaneously over several days using selective plane illumination microscopy (SPIM). The resulting large imagery dataset of several terabytes was processed in an automated manner on a high-performance computer cluster and segmented using a novel segmentation approach that uses images of red blood cells as training data. This analysis yielded a precise quantification of growth characteristics of the whole vascular network, head vasculature and tail vasculature over development. Our multi-sample platform demonstrates effective upgrades to conventional single-sample imaging platforms and paves the way for diverse quantitative long-term imaging studies.

KEY WORDS: Multi-sample imaging, Light sheet microscopy, Zebrafish, SPIM, Vasculature, Segmentation, Growth models

INTRODUCTION

The cardiovascular system is among the earliest functional organs to be formed during vertebrate development. From a few individual mesodermal precursor cells, a complex network of vessels forms through a variety of morphogenetic processes (Ellertsdóttir et al., 2010; Gore et al., 2012). Although many molecules involved in its formation have been identified (Adams and Alitalo, 2007; Gore et al., 2012; Hogan and Schulte-Merker, 2017), much remains unknown about how this intricate network comes into shape at the whole embryo level. A particularly exciting unanswered question is how the volume of the vascular system changes over development. Vascular volume is a strong proxy for overall vascular system size and consequently its development provides insight into

fundamental aspects of tissue development and whole-embryo morphogenesis. Here, we show how a combination of dedicated multi-sample preparation, comprehensive imaging and data processing, a novel segmentation approach, and growth data analysis provide a precise and quantitative characterization of embryonic vascular volume development.

To understand vascular formation at the whole-embryo level, the zebrafish has become a very valuable tool with many available vascular transgenic lines (Chávez et al., 2016). Compared with other vertebrate model organisms such as mice, the development of zebrafish is fast and takes place outside of the mother, and the optical translucency of zebrafish embryos provides an ideal setting for long-term *in vivo* time-lapse imaging experiments (Kimmel et al., 1995).

For long-term live imaging of zebrafish embryos and larvae, light sheet microscopy (Huiskens et al., 2004; Keller, 2013) has become the method of choice due to its illumination and detection scheme, which provides minimal photo-bleaching and phototoxicity (Daetwyler and Huiskens, 2016; Icha et al., 2017; Power and Huiskens, 2017). Moreover, light-sheet microscopy offers sample rotation in the microscope for multi-view imaging and tiling for full-embryo coverage (Weber and Huiskens, 2012), which is a necessity for imaging the entire vascular system. In addition, imaging zebrafish embryos over several days requires a sample embedding technique that provides mechanical constraints to ensure proper sample orientation but at the same time does not limit oxygen access or restrict growth. For single samples, an embedding method using fluorinated ethylene propylene (FEP) tubes (Kaufmann et al., 2012) has been widely accepted. However, to quantitatively analyse the observed processes, several samples need to be imaged. Ideally, these are imaged in one experiment simultaneously, which is especially important and efficient if the experiment takes several days to complete. Therefore, multi-sample imaging is highly desirable for long-term imaging studies.

The number of samples during imaging can be increased either by delivering samples with flow (Gualda et al., 2015; Regmi et al., 2013; Regmi et al., 2014; Wu et al., 2013) or by embedding multiple samples at the same time (de Luis Balaguer et al., 2016; Schmid et al., 2013). Delivering samples by flow does not offer the precise control of sample orientation needed for optimal image quality and comparison of different time points. Therefore, multi-sample embedding solutions are more promising for long-term imaging studies. However, existing multi-sample embedding solutions are currently only suitable for embryos still in their protective envelope, the chorion (Schmid et al., 2013), but not for growing zebrafish larvae. Sample holders for several plants have been designed to allow plant growth in near physiological condition (de Luis Balaguer et al., 2016) but do not provide sample rotation during imaging to access the entire sample. Therefore, the challenge is to develop a multi-sample embedding technique that allows for multi-view imaging.

¹Max Planck Institute of Molecular Cell Biology and Genetics, 01307 Dresden, Germany. ²Department of Cell Biology, UT Southwestern Medical Center, Dallas, TX 75390, USA. ³Center for Systems Biology Dresden, 01307 Dresden, Germany. ⁴Chair of Scientific Computing for Systems Biology, Faculty of Computer Science, TU Dresden, 01069 Dresden, Germany. ⁵Virtual Technology and Design, University of Idaho, Moscow, ID 83844, USA. ⁶Morgridge Institute for Research, Madison, WI 53715, USA. ⁷Department of Integrative Biology, University of Wisconsin, Madison, WI 53706, USA.

*Authors for correspondence (kharrington@uidaho.edu; jhuiskens@morgridge.org)

© S.D., 0000-0002-7444-4734; U.G., 0000-0002-1179-8228; C.D.M., 0000-0001-9940-0730; K.H., 0000-0002-7237-1973; J.H., 0000-0001-7250-3756

This is an Open Access article distributed under the terms of the Creative Commons Attribution License (<https://creativecommons.org/licenses/by/4.0>), which permits unrestricted use, distribution and reproduction in any medium provided that the original work is properly attributed.

A further complication arises when imaging several embryos simultaneously, as data handling becomes more challenging, with datasets easily exceeding several terabytes in size. Furthermore, such datasets comprise many acquisition volumes, angles and time points over multiple samples. It is consequently not possible to load an entire experiment into computer memory to inspect the data and apply conventional data processing and visualization workflows. Therefore, custom data processing tools are needed to automatically generate 3D stitched datasets for further analysis, and to visualize the acquired data for easy inspection.

Next, for an accurate description of vascular volume changes, visual inspections and qualitative analysis are not sufficient. Instead, quantitative measurements based on vascular segmentation are required. Most segmentation approaches in developmental biology focus on analysing nuclei and cytoplasmic content (Amat et al., 2014), but segmentation of the vasculature is more challenging because of the variety of vessel sizes, intensity changes over vessel walls and, most importantly, due to the hollow-tube structure of vessels. Therefore, no reliable segmentation of endothelial signal over long time periods has been established yet. To help with segmentation, micro-angiography (Isogai et al., 2001) is often used, in which a fluorescent dye is injected into the vasculature. However, at early developmental stages, the vasculature is not completely closed and dye rapidly leaks into the surrounding tissue, rendering microangiography not applicable for long-term developmental studies. A novel strategy of vascular segmentation is therefore required to extract quantitative growth measurements of the whole vasculature.

To interpret the quantitative measurements resulting from the complete multi-sample imaging and processing platform, there are many established mathematical growth models available (Hernandez-Llamas and Ratkowsky, 2004; Tsoularis and Wallace, 2002), such as the Gompertz model (Gompertz, 1825), logistic growth model (Verhulst, 1838), the Weibull model (Ratkowsky, 1983) or Richards' model (Richards, 1959; Tjørve and Tjørve, 2010). However, none of these models is capable of sufficiently describing our data. We therefore suggest a new class of growth models based on logarithmic rescaling of time to describe embryonic vascular development.

RESULTS

Multi-sample preparation for long-term time-lapse imaging

Successful vascular imaging relies on immobilization of the sample and mechanically constraining it to the field of view through embedding. In contrast to the widely established zebrafish embedding protocol for light sheet microscopy (Kaufmann et al., 2012), we abstained from using tricaine. Instead, to immobilize the embryos, we injected them with α -bungarotoxin RNA (Swinburne et al., 2015) at the one-cell stage. To embed several samples for simultaneous long-term imaging, we adapted the established protocol of single-embryo embedding. We first embedded individual zebrafish embryos in 0.1% agarose inside of FEP tubes for long-term imaging as described previously (Kaufmann et al., 2012) (Fig. 1A, Figs S1 and S2). These FEP tubes were cut to a length of about 8 mm and several of them were attached with other larger FEP tubes as connectors (Fig. 1B). Holes in these connectors ensured exchange of oxygen and liquids during imaging. This embedding technique was readily available, flexible and provided stable embedding of up to five fish for simultaneous, long-term imaging in one tube assembly with a length of about 6 cm (Fig. S3). A detailed step-by-step protocol for multi-sample embedding can be found in the supplementary Materials and Methods. We also include

suggestions for how to solve potential embedding problems (Table S1) and a detailed list of required embedding materials (Table S2).

To ensure that the multi-sample embedding did not compromise growth, we measured the overall body length of freely swimming zebrafish, single-sample and multiple-sample preparations over time, and compared their growth curves (Fig. 1C). Until 24 h after embedding [48 h post fertilization (hpf)], no growth difference was detected (ANOVA analysis, P -value 0.1721). This changed at 72 hpf (ANOVA analysis, P -value 0.0013), when the embedded fish were 5% smaller than the freely swimming fish after 2 days of embedding. However, the data provided no evidence that there was a growth impairment of the multi-sample embedded fish compared with the established one-sample embedding technique (two-sided t -test between one-sample and multi-sample embedding: $P=0.06$ at 72 hpf, 0.93 at 96 hpf and 0.98 at 120 hpf). Moreover, no additional growth defects such as oedemas were detected by visual inspection (Fig. S4).

Hardware adaptations for multi-sample imaging

The new 6 cm long tube assembly containing the embedded zebrafish embryos did not fit on our custom and other commercially available light-sheet microscopes. Therefore, we decided to upgrade an existing custom three-lens mSPIM microscope (Huiskens and Stainier, 2007) that has been successfully used in long-term imaging studies (Lenard et al., 2015). The existing mSPIM microscope was equipped with two illumination arms and one orthogonal detection arm. Furthermore, its rotational stage allowed us to rotate zebrafish embryos and image them from optimal angle(s) for better penetration and coverage. To upgrade this custom system, we designed a new translational stage system (Fig. 1D), with larger travel ranges to move every one of the five samples into the microscope's field of view. Furthermore, the depth and height of the sample chamber (Fig. 1E) was increased to provide enough space for the longer tube assembly. The taller chamber was 3D printed (Fig. 1E), making the chamber a cost-effective and easily adaptable unit. We incorporated in- and outlets for a perfusion system into the sample chamber to allow for temperature control of the medium and sample.

Multi-sample imaging of several zebrafish embryos

To study the development of the vascular volume, we simultaneously imaged five zebrafish embryos expressing a green fluorescent vascular endothelial marker, *Tg(kdr1:EGFP)* (Jin et al., 2005), and a red blood cell marker, *Tg(GATA1a:dsRed)* (Traver et al., 2003). The green fluorescent marker labelled the vessel walls and thus the outlines of the vascular system. The red blood cell marker labelled erythrocytes and thus provided information about the inside of the vasculature. To achieve optimal coverage of the entire vascular system, we chose three optimal angles for imaging (Fig. S5): to capture a good view on the head vasculature, we imaged the embryos with dual-sided illumination with the detection oriented dorsally; to achieve a good whole-embryo view, we imaged the zebrafish from two opposite angles $\pm 60^\circ$ rotated in the sagittal plane with single-sided illumination.

For acquisition, we used EMCCD cameras with a chip size of 960×960 pixels corresponding to a small 1.097×1.097 mm field of view when using our $10\times$ lens. As the embryos grew to a size of about 3.5 to 4 mm at 5 dpf, several acquisition volumes were required to reconstruct the whole embryos. In total, together with an overlap of about 30% for reliable data stitching, five acquisition volumes were needed to image one whole embryo from one angle.

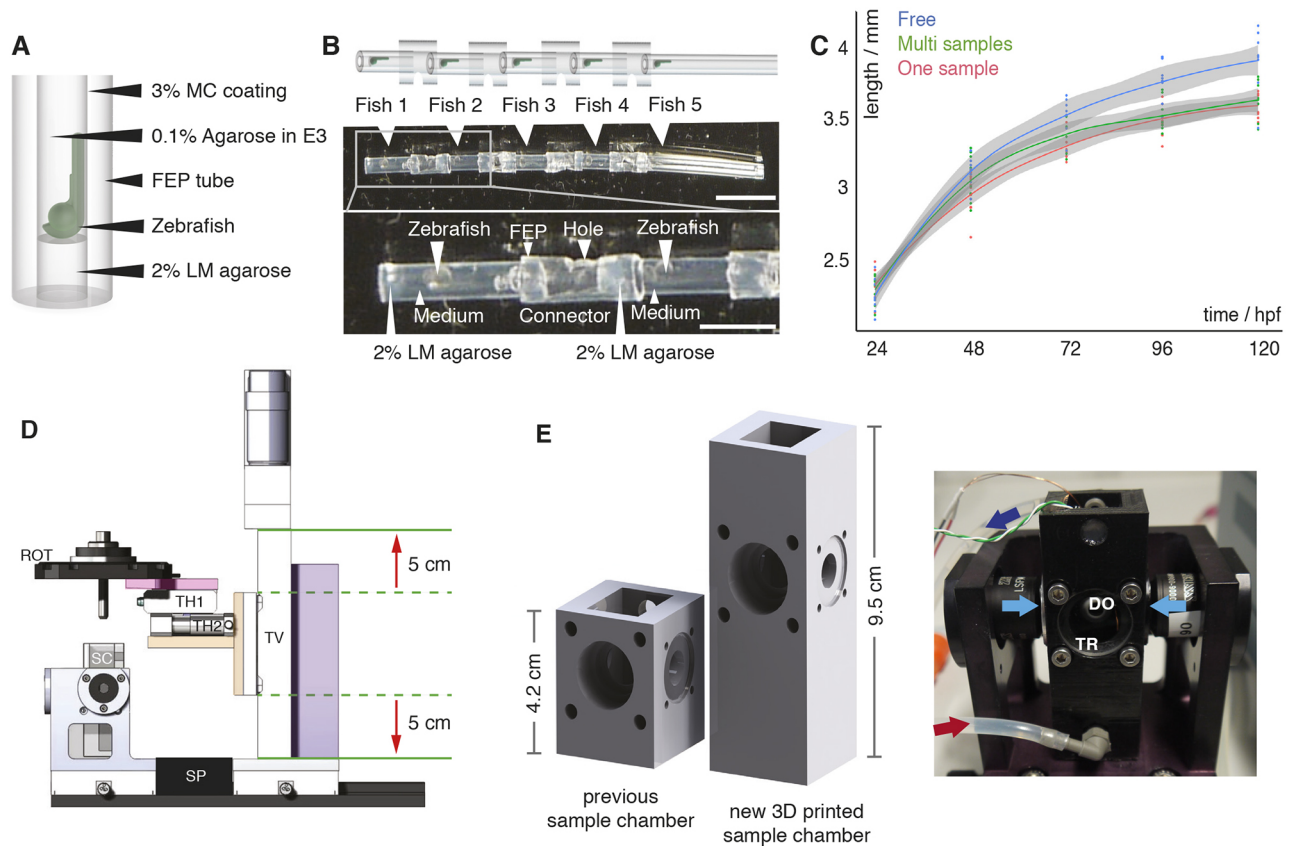


Fig. 1. Multi-sample embedding and necessary microscope modifications. (A) Schematic of single zebrafish embryo embedding in a fluorinated polypropylene (FEP) tube using 2% low melting point (LM) agarose as a plug, 0.1% agarose in E3 as the medium and 3% methylcellulose (MC) for coating the FEP tube, as described previously (Kaufmann et al., 2012). (B) Schematic (top) and images (middle) of five mounted zebrafish (white arrowheads) in FEP tube pieces assembled using FEP connectors. The bottom image shows details of the embedding: zebrafish mounted in the FEP tubes rested on a 2% LM agarose plug and were embedded in E3 medium containing 0.1% agarose. FEP tubes containing a single zebrafish embryo were attached with FEP connectors containing a hole. Scale bar: 1 cm (top image); 4 mm (bottom image). (C) Growth curve of freely swimming fish (blue, $n=8$), individually embedded samples (red, $n=10$) and samples embedded in the multi-sample tube (green, $n=9$) with the 0.95% confidence interval of Loess interpolation in grey. (D) The new translational stage design of the multi-sample imaging platform ensured a vertical travel range of 10 cm (red arrows) and was built with custom-made parts, e.g. an adapter (pink) between the rotational stage (ROT) and the translational stage platform, an adapter (orange) between the horizontal translational stages (TH1 and TH2) and the vertical translational stage (TV), and a stage mount (purple). SP, spacer; SC, sample chamber. (E) Comparison of a traditional one-sample SPIM chamber with the new 3D-printed sample chamber and a picture of the new sample chamber connected to a perfusion system with inflow (red arrow) and outflow (dark blue arrow), the two illumination objectives for dual-sided illumination (light-blue arrows), a window for transmission (TR), and a detection objective (DO) in the back.

Therefore, for imaging five embryos from three angles, 75 acquisition volumes were required. To capture the total 3D volume, we imaged every acquisition volume with at least 200 z-planes separated by 4 μ m.

To image the development of the vascular volume over time, we began imaging at around 17 hpf when the cells started to fuse to larger vessels by *in situ* aggregation of angioblasts (Ellertsdóttir et al., 2010), and imaged the entire developing vasculature every 20 min over a time period of at least 3 days. With these settings (75 acquisition volumes, dual-colour 16-bit images, 200 planes/acquisition volume, time step of 20 min), the corresponding data generation rate amounted to ~ 3.5 TB/day.

Microscope software adaptations for multi-sample imaging

The high data rate from our multi-sample imaging SPIM instrument posed a considerable challenge, as hard-drives available for the microscope had a total capacity of only 6 TB, making a 3-day time-lapse experiment impossible. We therefore decided to copy the accumulated data from every time point to a large, central storage unit in between acquisitions (see Materials and Methods, Fig. S6). This approach also eliminated the usual time-consuming data transfer at

the end of an experiment, which prevents the immediate start of the following experiment. Copying data during an experiment thus also increased the overall throughput of the microscope.

We further implemented an automated mosaic generation tool, because manually configuring a high number of individual acquisition volumes for each experiment is very time consuming and error prone. Given a starting position, e.g. the head of the fish, the other acquisition volumes were automatically determined with a 30% overlap, ensuring reliable stitching during data processing. The overall number of acquisition volumes was selected based on the expected growth of the zebrafish over the course of the time-lapse at the start of the experiment.

Dedicated processing pipeline

Multi-sample acquisition over 3 days as described above resulted in large datasets of over 10 TB with a convoluted data structure comprising many acquisition volumes, several angles and fish, and two channels. Using custom modular ImageJ/Fiji plug-ins (Schindelin et al., 2012), we transformed the raw data into a dataset that contained one stitched 3D stack per timepoint, channel, angle and fish (Figs S7, S8). Furthermore, to visually check the data quality, we

generated maximum intensity projections that also enabled a qualitative description of the formation of the vasculature (Movies 1 and 2). We adapted the plug-ins for use on a high-performance cluster for fast processing (supplementary Materials and Methods). Using the microscope stage parameters, we also automated all processing steps so that in the end only the folder of the experiment had to be given by the user. The code for all processing plug-ins is freely available at github.com/DaetwylerStephan/multi_sample_SPIM.

Segmentation of the vascular data

To quantitatively measure the vascular volume changes over time, a segmentation of the vasculature (Fig. 2A) was required. To provide an effective segmentation, we designed a novel approach (Fig. 2B) by complementing the signal of the endothelial marker with the signal from the red blood cell marker *Tg(gata1a:DsRed)*. We included the second marker because red blood cells circulate inside the vasculature and are therefore inherent proxies for a luminal marker. This provided ideal training data for a machine learning-based approach of vascular segmentation.

To establish the training set for solving the segmentation, we determined candidate locations for each individual 3D stack. Those locations were selected by taking the conjunction of the vasculature channels (Fig. 2C) and the thresholded red blood cell (Fig. 2D). Sample points were chosen by randomly sampling candidate coordinates and collecting the first N positive points and first N negative points without replacement ($N=5000$). The sample points were used as a target for the parameter fitting procedure.

For every sample point, the features from the vascular marker were extracted using first-order moments calculated with *ImgLib2* (Pietzsch et al., 2012). The features encoded the original image (Fig. 2C, feature 1), X, Y and Z gradients (Fig. 2C, feature 2-4) of the vasculature channel, the total gradient magnitude (Fig. 2C, feature 5), and an inverse-gradient weighted version of the original image (Fig. 2C, feature 6). The feature vectors for all sample points were then composed as a matrix and a target vector was generated, representing the positive/negative labels of training points as 1 and 0, respectively. Singular value decomposition was then used to solve for the segmentation parameters, i.e. a set of feature weights that maximized predictions of the target vector value.

The feature weights obtained from solving the linear fitting procedure were then used to compute an image of segmentation scores. Images were segmented by first using the fitted feature weights to compute a linear combination of the feature maps. The resulting image encoded the segmentation score for each voxel. The segmentation score image was then thresholded using the Triangle algorithm (Zack et al., 1977), resulting in a binary labelling of the image. A morphological erosion followed by a dilation filtered out single-pixel fragments.

With this novel segmentation approach in hand, the various challenges of vessel segmentation posed by vessel geometry and characteristics of the fluorescent marker (Fig. 2E) were overcome. The segmentation approach resulted in a segmentation that was capable of capturing even fine morphological details of vascular structures (Fig. 2E,F, Fig. S9).

As the segmentation had to cope with terabytes of data from the many unlabelled 3D stacks, we implemented our efficient and fully automated image segmentation pipeline in *FunImageJ* (Harrington et al., 2018). *FunImageJ* was used with a standard distribution of *Fiji* (Schindelin et al., 2012), and as a standalone program on a high-performance computing cluster to enable parallel processing of whole datasets. The resulting segmentations were then used to quantify growth of the vascular system over several days (Fig. 2G).

Vascular growth curve rates

With the segmentation in hand (Fig. 3A), quantifying the overall growth of the vascular system was a straightforward process of computing the number of segmented voxels in isotropic 3D stacks. To temporally align the volume measurements of different fish, we selected the anastomoses of the left and right primordial hindbrain channel (PHBC) as reference points.

The resulting quantitative data revealed that the growth of the vascular volume could be well described by a group of models relying on logarithmic rescaling of time, including the scaled cumulative log-logistic (Fig. 3B) and the scaled cumulative log-normal growth models (Fig. S10). To account for a limited time window of observation, a scaling parameter and an offset were introduced in both models. The offset A described the lower asymptote, i.e. the vascular volume already formed at the start of an imaging experiment. The scaling factor V_L described the upper asymptote, i.e. the maximum volume reached during the observed development. In addition, for the scaled cumulative log-logistic model, the scale parameter α and the shape parameter β were required to describe vascular volume growth (Fig. 3C). For the scaled cumulative log-normal growth model, two parameters μ (mean) and σ (standard deviation), which define the underlying log-normal function, were required. Consequently, in total only four parameters were required to model the development of the vascular volume over time. We used non-linear minimization to obtain the fitting parameters for both models (Table 1).

We compared the scaled cumulative log-normal and log-logistic growth model with other established growth models by calculating the residual sum of squares (RSS). A small RSS indicates a good fit to the data. The comparison of the RSS values revealed that the scaled cumulative log-normal and log-logistic growth models of the whole vasculature volume growth exceeded other established growth models, such as the Gompertz model (Gompertz, 1825), logistic growth (Verhulst, 1838), the Weibull model (Ratkowsky, 1983) or Richards' model (Richards, 1959; Tjørve and Tjørve, 2010) (Table 1, Fig. S11). Moreover, visual inspection of the residuals of the scaled cumulative log-normal and log-logistic growth model also indicated that those models fit best (Fig. S11).

To understand whether the overall growth characteristics of the whole vasculature were reflected in the growth of its subnetworks, such as the head or tail vasculature, we established a manually curated annotation of the vasculature (Movie 3). The volume changes of the differently annotated regions were determined by computing the number of segmented voxels with the corresponding annotation label in isotropic 3D stacks. The analysis of vascular volume development of the head and tail vasculature (Fig. 3C) revealed that they were also well described by the scaled cumulative log-logistic and log-normal models. The fitting parameters for both models were obtained by linear minimization and revealed a good fit (Table 1).

We inserted the above obtained parameters into the scaled log-logistic function on which the scaled cumulative log-logistic model was based (Fig. 3B). The scaled log-logistic function was the derivative of the scaled cumulative log-logistic model and thereby revealed the growth rate of the vascular volume (Fig. 3D). The maximal growth rate obtained was around 26 hpf for the whole vasculature, 27 hpf for the head and 29 hpf for the tail vasculature. Before this, the growth rate rapidly increased then, after reaching the maximum, the growth rate slowly decreased. Inserting the parameters of the scaled cumulative log-normal model into its derivative revealed the same values for whole vasculature and head vasculature, and 28 hpf for the tail vasculature (Fig. S10B).

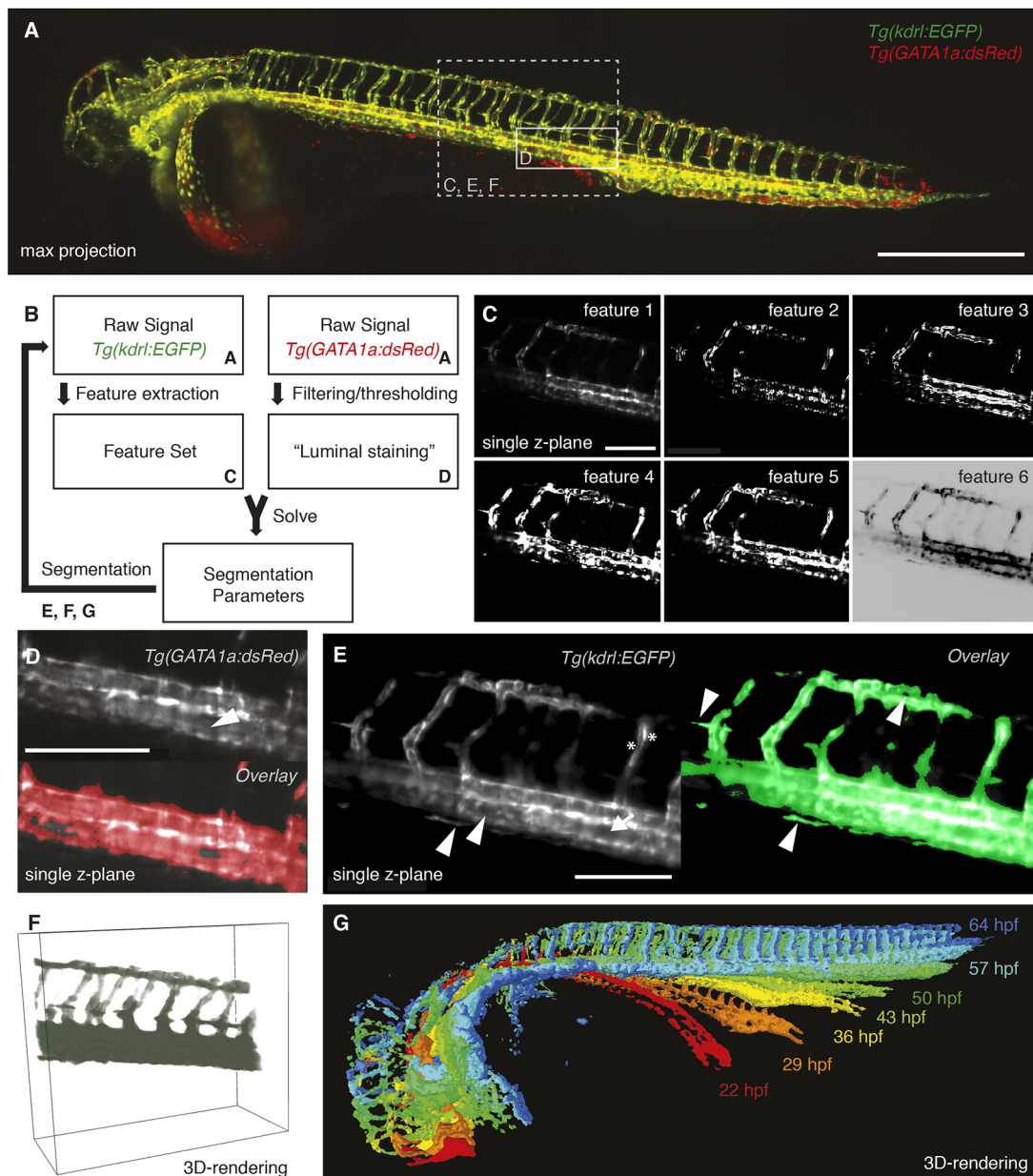


Fig. 2. Segmentation of the vascular data. (A) Maximum intensity projection of a zebrafish expressing the endothelial marker *Tg(kdr):EGFP* in green and the red blood cell marker *Tg(GATA1a:dsRed)* in red with boxes depicting selected regions shown in C-F. Scale bar: 500 μ m. (B) Schematic of the segmentation process with references to the corresponding figure panels (A,C-G). For successful segmentation, the imagery data of two channels was required: the raw data of the vascular marker *Tg(kdr):EGFP* and of the red blood cell marker *Tg(GATA1a:dsRed)* (A). (C) From the vascular marker, a feature set (C) was extracted. By filtering and thresholding the images of the red blood cell marker, a proxy for a luminal staining was established. The weights for the different features (segmentation parameters) were then calculated by using the luminal proxy as ground truth in a machine learning-based approach. With the obtained feature weights, the segmentation of the vascular channel was achieved. Features extracted from the endothelial marker *Tg(kdr):EGFP* included the raw signal (feature 1), gradient x (feature 2), gradient y (feature 3), gradient z (feature 4), total gradient (feature 5) and the inverse gradient weighted raw image (feature 6). Scale bar: 150 μ m. (D) Single plane of a 3D stack of the red blood cell marker *Tg(GATA1a:dsRed)* (top). As the red blood cells circulate in the vasculature, the interior of vessels was also filled with fluorescent signal (white arrowhead). Therefore, filtering and thresholding of the red blood cell marker raw signal (top) provided a ground truth (bottom, red) of signal inside the vasculature from which the segmentation parameters could be calculated. Scale bar: 150 μ m. (E) Single plane of a 3D stack of the endothelial marker (left) highlighting the challenges of vascular segmentation: hollow tubes (arrow), intensity differences (asterisks) and small vessels next to a large vessel (arrowheads). Using our segmentation approach (right), even fine structures of the vasculature were segmented correctly (arrowheads). Scale bar: 150 μ m. (F) 3D rendering of the selected region with the segmentation in green. (G) 3D rendering of the segmentations at different time points of development.

DISCUSSION

We have presented a dedicated and complete workflow of multi-sample preparation, multi-sample imaging, data processing and quantitative analysis of the vascular volume. Several key innovations in all those disciplines were necessary: we introduced

a new multi-sample embedding protocol, an upgraded light sheet microscope, a comprehensive library of data processing plug-ins, a novel vascular segmentation approach using inherent biological markers and new growth models relying on logarithmic rescaling of time for describing the development of embryonic vascular volume.

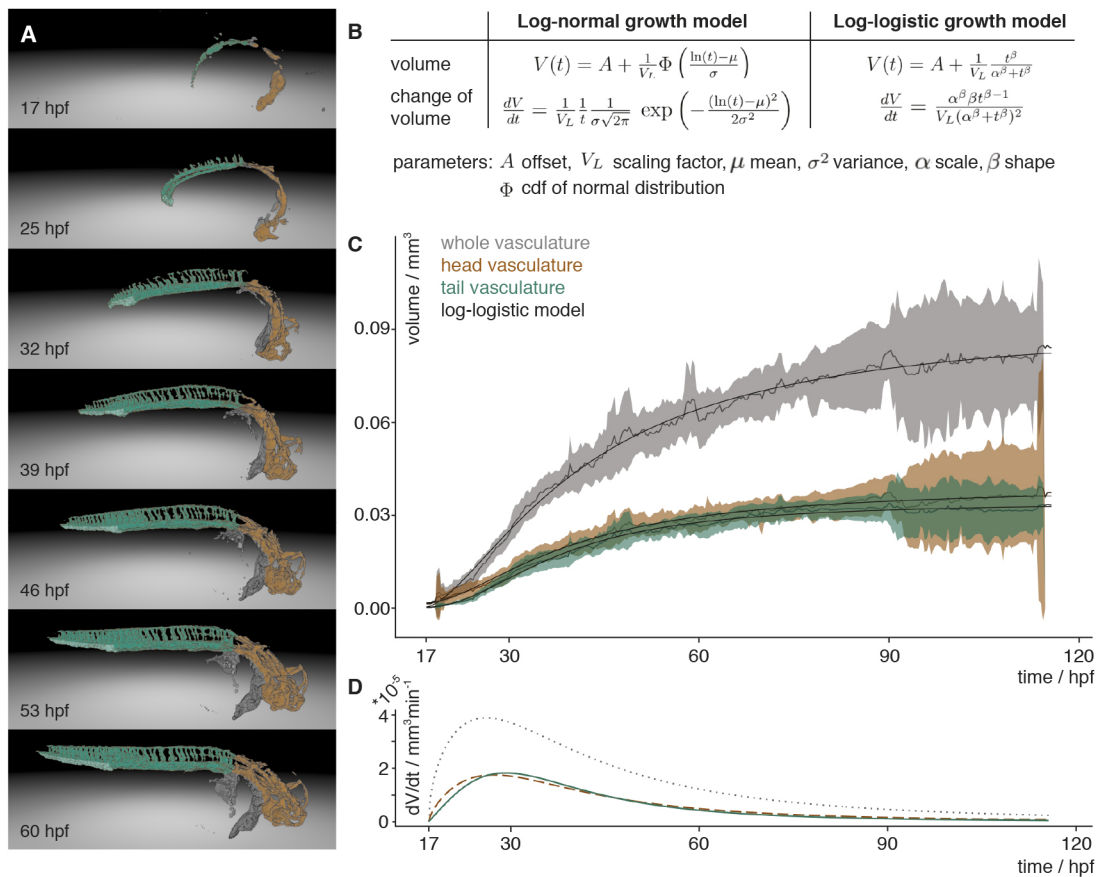


Fig. 3. Vascular volume growth characteristics of zebrafish. (A) Segmentation of the vasculature at seven different time points labelled with the annotation of the head (orange) and tail (turquoise) with its caudal vein plexus (light turquoise) and the rest of the segmented vasculature (grey). (B) Equations of the scaled cumulative log-logistic and log-normal growth models describing the volume $V(t)$ and change of volume dV/dt over time t with offset A , scaling factor V_L , mean μ and standard deviation σ of log-normal distribution and cumulative distribution function (cdf) Φ of the standard normal distribution, and log-logistic scale parameter α and shape parameter β . (C) Experimental measurements of the volume over time of the whole vasculature (grey), and the head (brown) and tail (turquoise) vasculature. The mean of the measurements is depicted with a solid line and the 95% confidence interval (t-statistics, $n=7$) as a ribbon in the corresponding colour. The black line depicts the approximation of the volume calculated using the scaled cumulative log-logistic growth model. The corresponding panel for the scaled cumulative log-normal model is in Fig. S10A. (D) The volume growth rate of the whole vasculature (grey, dotted), and head (brown, dashed) and tail (turquoise) vasculature was calculated by inserting the parameters obtained from the approximation into the change of volume equation of the scaled log-logistic growth model. The corresponding panel for the scaled log-normal model is in Fig. S10B.

The presented tools will further open the door for many other long-term imaging studies in fields such as developmental biology or xenograft models in cancer biology.

Growth of the vasculature

With our multi-sample imaging and analysis platform, we obtained a high-quality data set describing the growth of the vascular volume

Table 1. Growth model parameters to describe vascular growth

Model	Region	A (mm ³)	V_L (mm ⁻³)	μ [LN] α (min) [LL]	σ [LN] β [LL]	RSS \pm s.d. $\times 10^{-4}$ (mm ⁶)
LN	Whole vasculature	0.0019	11.36	7.309	1.013	8.1 \pm 0.7
LL	Whole vasculature	0.0004	10.87	1519	1.533	8.6 \pm 0.7
LN	Tail vasculature	0.0008	30.61	7.132	0.781	2.0 \pm 0.2
LL	Tail vasculature	0.0003	29.51	1271	2.006	2.1 \pm 0.2
LN	Head vasculature	0.0023	27.86	7.216	0.921	2.3 \pm 0.2
LL	Head vasculature	0.0017	26.75	1380	1.696	2.3 \pm 0.2
Gompertz	Whole vasculature	n.a.	n.a.	n.a.	n.a.	11.3 \pm 0.9
Richards'	Whole vasculature	n.a.	n.a.	n.a.	n.a.	11.3 \pm 0.9
Logistic	Whole vasculature	n.a.	n.a.	n.a.	n.a.	42.7 \pm 3.4
Weibull	Whole vasculature	n.a.	n.a.	n.a.	n.a.	10.8 \pm 0.9

Fitted parameters of the scaled cumulative log-normal (LN) and log-logistic (LL) growth models obtained by non-linear optimization described the vascular volume growth data (whole embryo, and tail and head vasculature) well. The parameters included the offset A (LN and LL), scaling factor V_L (LN and LL), mean μ [LN], scale α (LL), variance σ [LN] and shape β [LL]. The goodness of the fit was described by the residual sum of errors (RSS), with a low value indicating a good fit. The scaled cumulative log-normal and log-logistic growth model thereby outperformed other established growth models such as the Gompertz, Richards', logistic and Weibull models. n.a., not applicable.

over time. Descriptive features of the observed time course include a slow growth at the beginning, a maximum volume growth rate at around 26–29 hpf and then a decline of the growth rate resulting in a saturating growth process. To describe this growth, we fit well-established growth processes, such as Gompertz's, Richards' and Weibull's models or log-logistic function (Table 1). We found that they did not reproduce the first hours of vascular development well. In searching for an alternative growth model, we found that the best growth models to explain the data all include an effective, logarithmic rescaling of time. Log-normal-like dynamics and log-logistic growth fit best, and are clearly distinguishable from other, non-logarithmic growth models, but not from one another. To our knowledge, this is the first time that such models have been shown to be applicable to developmental processes.

It is not surprising that both the log-normal and the log-logistic growth model describe the data well. For certain ranges of parameters, the shape of their underlying growth rates can be very similar in nature. This is also known from statistics where the analogous log-normal and log-logistic distributions can be applied to right skewed distributions, and an experimenter can choose any one of the two models to describe the data (Dey and Kundu, 2009). Methods to distinguish the two often involve analysing their probability density function (Raqab et al., 2017). In our case, however, only the cumulative function as volume measurement is given. Other methods that rely on the analysis of the tails of the distribution were not applicable, as the observed time of growth was not long enough to unravel effects from the tails of the functions. However, the log-logistic growth model has the advantage that it is more easily interpretable as it has a closed function for the cumulative function contrary to the log-normal growth model. The scaled cumulative log-logistic model thereby is closely related to the logistic equation that is often applied in description of population growth in biology (Verhulst, 1838) or cancer growth (Vaidya and Alexandro, 1982).

One might envision such logarithmic rescaling of time as arising from an effective 'clock' that is driven by an exponentially decaying resource. In vasculature development, we speculate that factors such as: (1) nutrient availability; or (2) gene expression could introduce this effect and explain the observed logarithmic rescaling of time. In (1), a limited store of nutrients is deposited by the mother and remains the predominant source of nutrients over the first few days of development. Assuming an exponentially decaying use of nutrients out of this store, if each growth step of the vasculature requires some constant threshold amount of nutrient to proceed, then the growth steps over time become logarithmically rescaled. In (2), gene expression could also introduce similar rescaling effects. Here, feedback loops in gene expression patterns would enforce dependence on the pattern at a previous time point, leading to an exponentially decaying concentration of expression products. Again, if each vascular development step requires a threshold amount of these products, then logarithmically rescaled times would result.

Growth of vascular subnetworks

The volume measurements of large subnetworks of the vasculature such as the head and the tail vasculature were also well described by scaled cumulative log-logistic and log-normal growth models. This indicates that those large subnetworks were also subject to the same growth constraints as the whole vasculature and explain, in part, the fractal nature of vasculature. However, these constraints might not apply to smaller subnetworks as they can draw from and

release resources to neighbouring parts of the network, e.g. by cell migration. Therefore, those smaller subnetworks might show different growth behaviours. Indeed, the caudal vein plexus located in the tail of the vasculature first expanded, then remodelled and, after 73 hpf, decreased in size (Fig. S12), and therefore did not follow a scaled cumulative log-logistic or log-normal growth curve.

Multi-sample capacity is desired and important

Simultaneous imaging of several samples offers higher efficiency, shorter overall experimental time and therefore lower costs than sequential image acquisition. Furthermore, it enables the study of embryos from the same parents, growing under exactly the same conditions. This is especially important for imaging mutant fish lines. Homozygous mutant fish are often not viable (Kim et al., 2011), and therefore heterozygous fish lines are grown. However, only one quarter of their progeny are homozygous for the mutation of interest and exhibit the phenotype. To observe its establishment, fish are ideally selected before a phenotype is observable. Consequently, multi-sample imaging is essential for studying mutant fish lines with high spatial and temporal resolution.

The ability to image many samples is also important for experiments that are time consuming in preparation and/or rely on the short-term availability of rare, restricted or otherwise difficult to obtain samples. Examples include patient-derived samples, xenotransplantation samples, observations of induced cancer cells or small-scale screens of selected compounds. Our multi-sample platform has already been applied successfully to such a study where the influence of the Rho-kinase inhibitor fasudil was investigated on drug-treated and non-drug-treated fish in the same experiment (Asokan et al., 2017preprint). In future, the platform will provide the required sample capacity to tackle more such projects.

Moreover, with the multi-sample platform, new studies will be possible that aim to understand the variation and robustness of biological structures for which a high sample number is important. Indeed, the vasculature of zebrafish also shows variation (Fig. S13). In future studies, our long-term time-lapse platform will be used to study how such patterns of variation are established, maintained and/or remodelled. We are confident that our segmentation approach will therefore be the starting point for such endeavours. As a demonstration of such a study, we have quantified the symmetry of the intersegmental vessel pairs along the anterior-posterior axis (Fig. S14). Interestingly, the degree of symmetry changes depending on the position along the anterior-posterior axis.

Integration is crucial

The power of our multi-sample imaging platform lies in the integration of all of the important steps of multi-sample imaging – sample preparation, imaging, data processing and data analysis – into a single dedicated pipeline to obtain quantitative data (Fig. 4). For example, the data analysis benefits from the right choice of sample. Only by using the red blood cells as a luminal marker, did we obtain good training data to solve for the segmentation parameters. In a further example, imaging and data processing are interlinked, as the acquisition parameters, here the translational stage positions, are crucial for reliable stitching. As all of our processing and analysis code is freely available, other researchers may adapt parts of the whole pipeline to their dedicated research question. Moreover, our suggested upgrade for multi-sample imaging may be easily incorporated into other custom-built systems, together with the embedding protocol described in detail

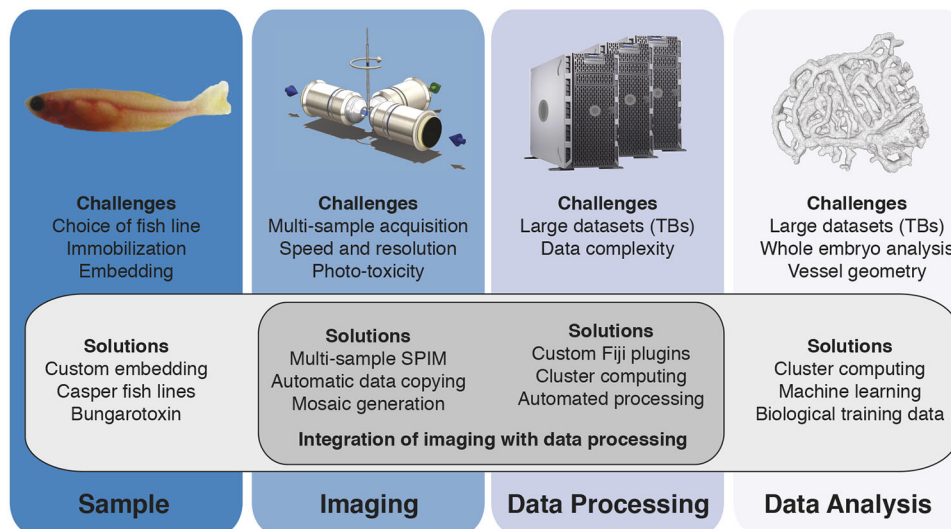


Fig. 4. A dedicated imaging, processing and analysis platform for multi-sample imaging. Integration of important steps of multi-sample imaging, such as sample preparation, imaging, data processing or data analysis, facilitates the individual steps and enables multi-sample imaging.

here. Hence, this toolset will help current imaging strategies move from qualitative descriptions of single observations to quantitative analysis over multiple samples.

MATERIALS AND METHODS

Ethics statement

The animal experiments were performed in accordance with the European Union (EU) directive 2011/63/EU as well as the German Animal Welfare Act.

Zebrafish sample preparation

Zebrafish (*Danio rerio*) adults and embryos were kept at 28.5°C and were handled according to established protocols (Nüsslein-Volhard and Dahm, 2002; Westerfield, 2000). To understand vascular growth in zebrafish, we compared *Tg(fli1a:EGFP)* (Lawson and Weinstein, 2002) and *Tg(kdr1:EGFP)* (Jin et al., 2005). As the marker *Tg(fli1a:EGFP)* was expressed not only in the head vasculature but more broadly in the head (data not shown), we decided to use *Tg(kdr1:EGFP)* and crossed this fish line into a casper background (White et al., 2008) to suppress formation of pigmentation. The *Tg(kdr1:EGFP)* casper fish line was crossed with the line *Tg(GATA1a:dsRed)* (Traver et al., 2003) expressing a fluorescent red blood cell marker. For time-lapse experiments, zebrafish embryos were injected at the one-cell stage with 30 pg of α -bungarotoxin RNA (Swinburne et al., 2015) to ensure immobilization during the time-lapse. A detailed step-by-step protocol for embedding the embryos for imaging is in the supplementary Materials and Methods.

Growth measurement

Freely swimming zebrafish, single-sample and multiple-sample preparations were set up at 24 hpf. Freely swimming zebrafish ($n=8$), single-sample ($n=10$) and multi-sample ($n=9$) preparations were then imaged using an AVT stingray camera connected to an Olympus SZX16 stereo microscope at 24, 48, 72, 96 and 120 hpf. To calibrate the length measurement, a PYSER-SGI stage micrometer (10 mm/0.1 mm) was imaged together with the zebrafish embryo. Fiji (Schindelin et al., 2012) was used to first calibrate and then measure the length of the zebrafish embryo.

In vivo time-lapse imaging

Long-term time-lapse imaging was performed on a custom-made multidirectional SPIM (mSPIM) setup (Huisken and Stainier, 2007) upgraded to multi-sample capacity (see Results section). The microscope was equipped with two Zeiss 10 \times /0.2 NA illumination objectives and an UMPlanFL N 10 \times /0.3 NA Olympus detection objective. Coherent Sapphire 488 nm and 561 nm lasers, each 100 mW maximum power, were used to

illuminate the sample. The images were recorded with two Andor DV885 iXon EM-CCD cameras. The embryos were imaged at least every 25 min for up to 4 days starting around 17 hpf.

Design of the translational stage system

The translational stage system of the microscope required high precision as it positioned the sample and scanned it through the light sheet. Therefore, a precise, translational stage with a longer travel range had to replace the existing vertical translational stage unit (Fig. 1D). We chose the M-404.4PD precision translation stage (Physik Instrumente) as it offered a unidirectional repeatability of 0.5 μ m, equal to half a pixel on the camera, and an overall travel range of 100 mm, which was sufficient for imaging several samples. To integrate the larger stage, we designed custom parts to connect the M-404.4PD stage to two M-111.1DG translational stages (Physik Instrumente) for lateral and axial scanning. We further added a solid metal block to stabilize the translational stage system and avoid vibrations caused by translational movements.

Data copying in-between timepoints

For data transfer, we used the Windows command line executable Robocopy that was started immediately after the acquisition of every 3D stack and copied data until just before a new stack acquisition was started. Robocopy was integrated into Labview, the microscope control software, using their executable interface framework. This ensured robust data transfer, as Robocopy only removed old data once the integrity of the file at the new server location was checked.

Data processing

Custom-made data processing tools in Fiji (Schindelin et al., 2012) were written to process the data from the microscope automatically. For visualization, the acquired fluorescence images were projected using maximum intensity projections. The resulting projections were stitched and fused with linear blending using custom code adapted from the Fiji stitching plugin by Stephan Preibisch et al. (Preibisch et al., 2009) that relies on phase correlation (Kuglin and Hines, 1975). For successful stitching (Fig. S8), we initialized the stitching with the translational stage positions. As the translational stages were very precise, the stitching was robust and determined globally for all timepoints. The stitching parameters of the maximum intensity projections were also applied to the 3D data to generate one 3D fused stack per timepoint, angle, fish and channel. While the different channels were already aligned optically, we used a manual GUI interface to obtain a precise fine alignment of the different channels using rigid registration. To reduce the amount of data for storage to about half the size, the data was compressed by zipping. Code of the custom-made processing steps is available freely at github.com/DaetwylerStephan/multi_sample_SPIM.

Segmentation

Segmentation of vasculature is particularly challenging because blood vessels are hollow tubes of widely varying diameters, often in very close proximity to each other. Additionally, endothelial markers often show heterogeneous densities across the vessel walls, e.g. with higher intensities around nuclei. Therefore, classical approaches such as filter-based approaches (Sato et al., 1998) or simple thresholding did not result in good segmentations (data not shown). Consequently, we have designed a novel approach of vessel segmentation (see Results section). The image segmentation software was developed using FunImageJ (Harrington et al., 2018), a Lisp-based interface for ImageJ. Code is freely available at: github.com/kephale/virtualfish-segmentation.

Visualization of segmentation

To visually check the quality of the segmentation (Fig. 2E), we overlaid the segmented images with the raw signal at selected timepoints. We further visually inspected all segmentations over the whole time-lapse course using maximum intensity projections and by 3D rendering (Fig. 2F,G, Movie 3) the segmentation and the annotations using SciView (available at github.com/scenerygraphics/sciview) or Vaa3D (Peng et al., 2010).

Quantification of vascular growth

For quantification of the segmentation, we rescaled each segmented 3D stack of a time-lapse series to isotropic resolution and then counted the number of segmented voxels. We quantified only the two opposite angles rotated by $\pm 60^\circ$ from the sagittal plane. Those two angles provided the best resolution of the whole zebrafish embryo vasculature. To obtain the vascular volume growth curves for one fish, the quantification result of both angles was averaged.

Annotation of the segmented vasculature

For the annotation, we used the maximum intensity projections of the endothelial signal over time. We first selected manually a region of interest, such as the caudal vein plexus, the head or the tail vasculature (including the caudal vein plexus), at the last timepoint of a time series. To automatically track this region of interest over time, we sequentially determined the region of interest at time $t-1$ given the region of interest at time t . For this, the boundary of the region of interest was discretized by points. For each point at time t , the corresponding point at time $t-1$ was determined. Assuming that only small-scale changes were present, the computation for each point was reduced by considering only a subregion of the image at time $t-1$ (140×140 pixels) as a search image for the template that was a small crop of the image at time t (70×70 pixels concentric around point). Within the search image, smaller images of the size of the template were created and compared against the template using image correlation. The position with the highest similarity was the new place for the boundary point. To increase robustness of the method, the shift vectors [new position at time ($t-1$)—position at time t] for each point were determined and the median over the seven neighbouring boundary points calculated and assigned as effective shift. Furthermore, if two boundary points were assigned to the same or neighbouring pixel, one of them was removed from the computation. To ensure the quality of the annotation, we visually inspected and curated the annotation.

Analysis of volume growth

The resulting volume measurements were analysed with the software package R (R Core Team, 2018) using the dplyr library package (Wickham et al., 2018) for data handling. Parameters for different growth models were optimized using non-linear regression of the sum of squared differences between the actual values and the predicted value of the growth model given the parameters. As optimization algorithm, we applied a non-linear least squares approach (nls function in R). In case nls failed, we applied the Levenberg-Marquardt algorithm (nlsLM function in R; Elzhov et al., 2016). Plots were generated using the ggplot library (Wickham, 2016) and the gridExtra package (Auguie, 2017).

Acknowledgements

We thank all members of the Huisken lab and the PhD advisory committee members Ingo Röder and Ivo Sbalzarini for constructive feedback and comments; the

computer department at MPI-CBG, especially Edmund Malik and Oscar Gonzales, for providing the computer infrastructure required for this project, the fish facility at MPI-CBG (Jens Hueckmann, Joachim Hellmig, Jürgen Müller and Evelyn Lehmann) for maintaining the fish lines; and the mechanical workshop at MPI-CBG (Hartmut Wolf and Falk Elsner) for producing the custom-made hardware.

Competing interests

The authors declare no competing or financial interests.

Author contributions

Conceptualization: S.D., J.H.; Methodology: S.D., U.G., C.D.M., K.H., J.H.; Software: S.D., U.G., K.H.; Validation: S.D.; Formal analysis: S.D., C.D.M.; Investigation: S.D., K.H., J.H.; Resources: S.D.; Data curation: S.D., K.H.; Writing - original draft: S.D.; Writing - review & editing: S.D., C.D.M., K.H., J.H.; Visualization: S.D., U.G., K.H.; Supervision: C.D.M., J.H.; Project administration: C.D.M., J.H.; Funding acquisition: C.D.M., K.H., J.H.

Funding

This work was funded by the Max-Planck-Gesellschaft and the Human Frontiers Science Program (CDA00063/2010). Deposited in PMC for immediate release.

Data availability

The code for all processing plug-ins is freely available at github.com/DaetwylerStephan/multi_sample_SPIM. The code for the segmentation is freely available at github.com/kephale/virtualfish-segmentation.

Supplementary information

Supplementary information available online at <http://dev.biologists.org/lookup/doi/10.1242/dev.173757.supplemental>

References

- Adams, R.H. and Alitalo, K. (2007). Molecular regulation of angiogenesis and lymphangiogenesis. *Nat. Rev. Mol. Cell Biol.* **8**, 464–478.
- Amat, F., Lemon, W., Mossing, D. P., McDole, K., Wan, Y., Branson, K., Myers, E. W. and Keller, P. J. (2014). Fast, accurate reconstruction of cell lineages from large-scale fluorescence microscopy data. *Nat. Methods* **11**, 951–958.
- Asokan, N., Daetwyler, S., Bernas, S. N., Schmied, C., Volger, S., Lambert, K., Wobus, M., Wermke, M., Kempermann, G., Huisken, J. et al. (2017). Continuous high-resolution in vivo imaging reveals tumor-specific dissemination in an embryonic zebrafish xenograft model. *bioRxiv*.
- Auguie, B. (2017). gridExtra: Miscellaneous functions for “grid” graphics [R package gridExtra version 2.3].
- Chávez, M. N., Aedo, G., Fierro, F. A., Allende, M. L. and Egaña, J. T. (2016). Zebrafish as an emerging model organism to study angiogenesis in development and regeneration. *Front. Physiol.* **7**, 56.
- Daetwyler, S. and Huisken, J. (2016). Fast fluorescence microscopy with light sheets. *Biol. Bull.* **231**, 14–25.
- de Luis Balaguer, M. A., Ramos-Pezzotti, M., Rahhal, M. B., Melvin, C. E., Johannes, E., Horn, T. J. and Sozzani, R. (2016). Multi-sample Arabidopsis Growth and Imaging Chamber (MAGIC) for long term imaging in the ZEISS Lightsheet Z.1. *Dev. Biol.* **419**, 19–25.
- Dey, A. K. and Kundu, D. (2009). Discriminating between the log-normal and log-logistic distributions. *Commun. Stat. Theory Methods* **39**, 280–292.
- Ellertsdóttir, E., Lenard, A., Blum, Y., Krudewig, A., Herwig, L., Affolter, M. and Belting, H.-G. (2010). Vascular morphogenesis in the zebrafish embryo. *Dev. Biol.* **341**, 56–65.
- Elzhov, T. V., Mullen, K. M., Spiess, A.-N. and Bolker, B. (2016). minpack.lm: R interface to the Levenberg-Marquardt nonlinear least-squares algorithm found in MINPACK, plus support for bounds. R package version 1.2-1.
- Franco, C. A., Jones, M. L., Bernabeu, M. O., Vion, A.-C., Barbacena, P., Fan, J., Mathivet, T., Fonseca, C. G., Ragab, A., Yamaguchi, T. P. et al. (2016). Non-canonical Wnt signalling modulates the endothelial shear stress flow sensor in vascular remodelling. *eLife* **5**, e07727.
- Gompertz, B. (1825). On the nature of the function expressive of the law of human mortality, and on a new mode of determining the value of life contingencies. *Philos. Trans. R. Soc. Lond. B Biol. Sci.* **515**, 513–585.
- Gore, A. V., Monzo, K., Cha, Y. R., Pan, W. and Weinstein, B. M. (2012). Vascular development in the zebrafish. *Cold Spring Harb. Perspect. Med.* **2**, a006684.
- Gualda, E. J., Pereira, H., Vale, T., Estrada, M. F., Brito, C. and Moreno, N. (2015). SPIM-fluid: open source light-sheet based platform for high-throughput imaging. *Biomed. Optics Express* **6**, 4447–4456.
- Harrington, K. I. S., Rueden, C. T. and Eliceiri, K. W. (2018). FunImageJ: a Lisp framework for scientific image processing. *Bioinformatics* **34**, 899–900.
- Hernandez-Llamas, A. and Ratkowsky, D. A. (2004). Growth of fishes, crustaceans and molluscs: estimation of the von Bertalanffy, Logistic, Gompertz and Richards curves and a new growth model. *Mar. Ecol. Prog. Ser.* **282**, 237–244.

- Hogan, B. M. and Schulte-Merker, S. (2017). How to plumb a pscis: understanding vascular development and disease using zebrafish embryos. *Dev. Cell* **42**, 567-583.
- Huiskens, J. and Stainier, D. Y. R. (2007). Even fluorescence excitation by multidirectional selective plane illumination microscopy (mSPIM). *Opt. Lett.* **32**, 2608-2610.
- Huiskens, J., Swoger, J., Del Bene, F., Wittbrodt, J. and Stelzer, E. H. K. (2004). Optical sectioning deep inside live embryos by selective plane illumination microscopy. *Science* **305**, 1007-1009.
- Isogai, S., Horiguchi, M. and Weinstein, B. M. (2001). The vascular anatomy of the developing zebrafish: an atlas of embryonic and early larval development. *Dev. Biol.* **230**, 278-301.
- Jaroslav, I., Weber, M., Waters, J. C. and Norden, C. (2017). Phototoxicity in live fluorescence microscopy, and how to avoid it. *BioEssays* **39**, 1700003.
- Jin, S.-W., Beis, D., Mitchell, T., Chen, J.-N. and Stainier, D. Y. R. (2005). Cellular and molecular analyses of vascular tube and lumen formation in zebrafish. *Development* **132**, 5199-5209.
- Kaufmann, A., Mickoleit, M., Weber, M. and Huiskens, J. (2012). Multilayer mounting enables long-term imaging of zebrafish development in a light sheet microscope. *Development* **139**, 3242-3247.
- Keller, P. J. (2013). In vivo imaging of zebrafish embryogenesis. *Methods* **62**, 268-278.
- Kim, S.-H., Speirs, C. K., Solnica-Krezel, L. and Ess, K. C. (2011). Zebrafish model of tuberous sclerosis complex reveals cell-autonomous and non-cell-autonomous functions of mutant tuberin. *Dis. Model. Mech.* **4**, 255-267.
- Kimmel, C. B., Ballard, W. W., Kimmel, S. R., Ullmann, B. and Schilling, T. F. (1995). Stages of embryonic development of the zebrafish. *Dev. Dyn.* **203**, 253-310.
- Kuglin, C. D. and Hines, D. C. (1975). The phase correlation image alignment method. In *Proc. of the IEEE Int. Conf. Cybernetics and Society*, 163-165.
- Lawson, N. D. and Weinstein, B. M. (2002). In vivo imaging of embryonic vascular development using transgenic zebrafish. *Dev. Biol.* **248**, 307-318.
- Lenard, A., Daetwyler, S., Betz, C., Ellertsdoth, E., Belting, H.-G., Huiskens, J. and Affolter, M. (2015). Endothelial cell self-fusion during vascular pruning. *PLoS Biol.* **13**, e1002126.
- Nüsslein-Volhard, C. and Dahm, R. (2002). *Zebrafish: A Practical Approach*. Oxford University Press.
- Peng, H., Ruan, Z., Long, F., Simpson, J. H. and Myers, E. W. (2010). V3D enables real-time 3D visualization and quantitative analysis of large-scale biological image data sets. *Nat. Biotechnol.* **28**, 348-353.
- Pietzsch, T., Preibisch, S., Tomančák, P. and Saalfeld, S. (2012). ImgLib2—generic image processing in Java. *Bioinformatics* **28**, 3009-3011.
- Power, R. M. and Huiskens, J. (2017). A guide to light-sheet fluorescence microscopy for multiscale imaging. *Nat. Meth.* **14**, 360-373.
- Preibisch, S., Saalfeld, S. and Tomancak, P. (2009). Globally optimal stitching of tiled 3D microscopic image acquisitions. *Bioinformatics* **25**, 1463-1465.
- R Core Team. (2018). *R: A Language and Environment for Statistical Computing*. Vienna, Austria.
- Raqab, M. Z., Al-Awadhi, S. A. and Kundu, D. (2017). Discriminating among Weibull, log-normal, and log-logistic distributions. *Commun. Stat. Simul. Comput.* **47**, 1397-1419.
- Ratkowsky, D. A. (1983). *Nonlinear Regression Modeling*. Dekker.
- Regmi, R., Mohan, K. and Mondal, P. P. (2013). MRT letter: light sheet based imaging flow cytometry on a microfluidic platform. *Microsc. Res. Tech.* **76**, 1101-1107.
- Regmi, R., Mohan, K. and Mondal, P. P. (2014). High resolution light-sheet based high-throughput imaging cytometry system enables visualization of intra-cellular organelles. *AIP Adv.* **4**, 97125.
- Richards, F. J. (1959). A flexible growth function for empirical use. *J. Exp. Bot.* **10**, 290-301.
- Sato, Y., Nakajima, S., Shiraga, N., Atsumi, H., Yoshida, S., Koller, T., Gerig, G. and Kikinis, R. (1998). Three-dimensional multi-scale line filter for segmentation and visualization of curvilinear structures in medical images. *Med. Image Anal.* **2**, 143-168.
- Schindelin, J., Arganda-Carreras, I., Frise, E., Kaynig, V., Longair, M., Pietzsch, T., Preibisch, S., Rueden, C., Saalfeld, S., Schmid, B. et al. (2012). Fiji: an open-source platform for biological-image analysis. *Nat. Methods* **9**, 676-682.
- Schmid, B., Shah, G., Scherf, N., Weber, M., Thierbach, K., Campos, C. P., Roeder, I., Aanstad, P. and Huiskens, J. (2013). High-speed panoramic light-sheet microscopy reveals global endodermal cell dynamics. *Nat. Commun.* **4**, 2207.
- Swinburne, I. A., Mosaliganti, K. R., Green, A. A. and Megason, S. G. (2015). Improved long-term imaging of embryos with genetically encoded α -bungarotoxin. *PLoS ONE* **10**, e0134005.
- Tjörve, E. and Tjörve, K. M. C. (2010). A unified approach to the Richards-model family for use in growth analyses: why we need only two model forms. *J. Theor. Biol.* **267**, 417-425.
- Traver, D., Paw, B. H., Poss, K. D., Penberthy, W. T., Lin, S. and Zon, L. I. (2003). Transplantation and in vivo imaging of multilineage engraftment in zebrafish bloodless mutants. *Nat. Immunol.* **4**, 1238-1246.
- Tsoularis, A. and Wallace, J. (2002). Analysis of logistic growth models. *Math. Biosci.* **179**, 21-55.
- Vaidya, V. G. and Alexandro, F. J. (1982). Evaluation of some mathematical models for tumor growth. *Int. J. Biomed. Comput.* **13**, 19-36.
- Verhulst, P. F. (1838). Notice sur la loi que la population suit dans son accroissement. *Correspondance mathématique et physique* 113-121.
- Weber, M. and Huiskens, J. (2012). Omnidirectional microscopy. *Nat. Methods* **9**, 656-657.
- Westerfield, M. (2000). *The Zebrafish Book. A Guide for the Laboratory use of Zebrafish Danio rerio*, 4th edn. Eugene: Univ. of Oregon Press.
- White, R. M., Sessa, A., Burke, C., Bowman, T., LeBlanc, J., Ceol, C., Bourque, C., Dovey, M., Goessling, W., Burns, C. E. et al. (2008). Transparent adult zebrafish as a tool for in vivo transplantation analysis. *Cell Stem Cell* **2**, 183-189.
- Wickham, H. (2016). *ggplot2: Elegant Graphics for Data Analysis*. New York: Springer-Verlag.
- Wickham, H., François, R., Henry, L. and Müller, K. (2018). dplyr: a grammar of data manipulation. R package version 0.7.6.
- Wu, J., Li, J. and Chan, R. K. Y. (2013). A light sheet based high throughput 3d-imaging flow cytometer for phytoplankton analysis. *Optics Express* **21**, 14474-14480.
- Zack, G. W., Rogers, W. E. and Latt, S. A. (1977). Automatic measurement of sister chromatid exchange frequency. *J. Histochem. Cytochem.* **25**, 741-753.

Supplementary Materials and Methods

Detailed embedding protocol

This supplementary chapter describes how to extend the embedding protocol established for mounting single embryos (Kaufmann et al., 2012; Weber et al., 2014) to multiple samples. Furthermore, potential difficulties and pitfalls of the embedding protocol are described and suggestions on how to solve them are provided.

1. Preparation for multi-sample embedding

The required material for embedding was prepared (Fig. S1) and kept at room temperature for at least 5 min. In-between experiments, the embedding material (except for the FEP tubes) was stored at 4 °C.

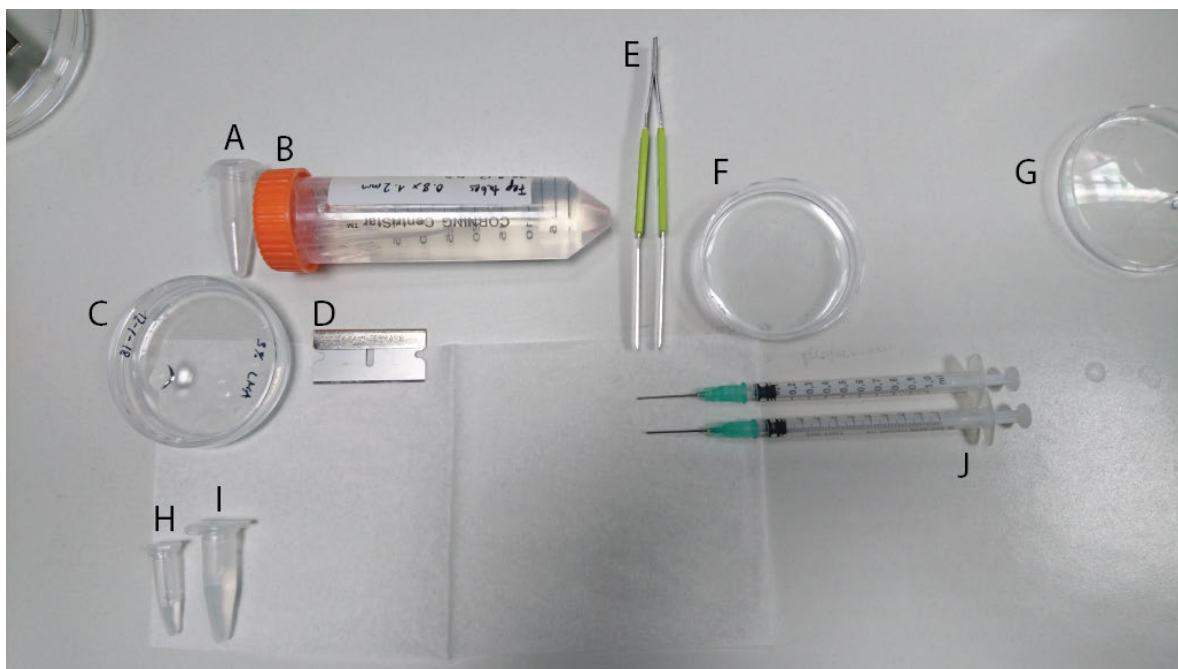


Fig. S1: Material required for multi-sample embedding

(A) Reaction tube containing reusable connectors, (B) centrifuge tube containing cleaned FEP tubes stored in distilled water, (C) dish containing a 2mm layer of 3% low melting agarose, (D) razor blade, (E) forceps, (F) dish with prepared samples, (G) dish with E3 to rinse coated FEP tubes, (H) tube containing 3% methylcellulose, (I) tube containing 0.1% agarose.

Zebrafish embryos

Zebrafish (*Danio rerio*) adults and embryos were kept at 28.5 °C and handled according to established protocols (Nüsslein-Volhard and Dahm, 2002; Westerfield, 2000). The fish lines of interest were crossed into a casper background (White et al., 2008) to improve image quality by the lack of pigmentation. Male and female zebrafish were set up with a divider, which was removed in the morning to time the mating of the fish. After mating, embryos were collected in a dish filled with E3 media.

The collected embryos were injected at the one or two cell stage with 2 nl of injection mix containing alpha-bungarotoxin RNA (Swinburne et al., 2015). Alpha-bungarotoxin immobilized

the embryos during imaging. The injection mix was prepared of 7.7 μ l distilled water, 2 μ l phenolred and 0.3 μ l of stock solution containing alpha-bungarotoxin RNA at a concentration of 500 ng/ μ l.

At around 15 hpf, the embryos expressing the fluorescent vascular marker of interest were prepared for imaging by dechoriation with sharp forceps under a stereomicroscope.

Fluorinated Ethylene Propylene (FEP) tubes

Fluorinated Ethylene Propylene (FEP) tubes with an inner diameter of 0.8 mm, and an outer diameter of 1.2 mm were cleaned according to established protocols (Kaufmann et al., 2012; Weber et al., 2014): First, the FEP tubes were flushed with 1M NaOH and then transferred to a 50ml centrifuge tube filled with 0.5 M NaOH and ultrasonicated for 10 min. After that, the tubes were flushed with distilled water and then with 70% ethanol. After flushing the tubes, they were ultrasonicated in 70% ethanol and cut to a length of about 4 cm.

If desired, the tubes were straightened before cutting. For this, FEP tubes were inserted into steel tubes of 50 cm length. The outer diameter of the FEP tubes matched the inner diameter of the steel tube. The tubes were heated to 180 °C for 2 h in an autoclave and afterwards cooled at room temperature for at least 5 h.

Connectors

FEP tubes with an inner diameter of 1.1 mm and an outer diameter of 1.5 mm were used as connecting FEP tube (connector). The slightly smaller inner diameter of the connector compared to the outer diameter of the FEP tube containing the sample (1.2 mm) ensured a tight fit. The connector was prepared by mounting the FEP tube on a blunt ended needle (1.2 mm x 40 mm). On this, a hole of about 2 mm was cut in the middle of the connector and the connector cut to its final length of about 6 mm. The connectors were reused in several experiments.

3% methylcellulose for coating

3% methylcellulose was prepared for coating the FEP tube to prevent attachment of the growing fish to the FEP wall. E3 was heated to approximately 60-70 °C and methylcellulose powder was added to a final concentration of 3%. To ensure a homogenous solution, it was stirred at 4 °C overnight.

0.1% agarose in E3 and 3% agarose dish for plugging

The appropriate amount of agarose was dissolved in E3 and heated up in a microwave until the agarose solution appeared homogeneous. 1.2 ml aliquots of 0.1% agarose were prepared in 1.5 ml reaction tubes and stored at 4 °C. Similarly, the 3% low melting agarose was poured into small petri-dishes (60 mm x 15 mm) to a thickness of about 2 mm. After solidification, E3 medium was added on top of the low melting agarose layer to prevent it from drying. Also, the petri-dish with the low melting agarose was stored at 4 °C.

2. Embedding of single samples

To embed multiple embryos, the protocol for single-sample embedding (Kaufmann et al., 2012; Weber et al., 2014) was followed. The use of gloves during the embedding procedure prevented contamination and impairment of imaging by finger prints on the tubes. Furthermore, bending the FEP tubes at this stage was avoided as the FEP tube might relax to its previous state during time-lapse imaging and consequently move the sample out of the field of view.

Coating of the FEP tube

First, the FEP tube was coated with 3% methylcellulose. The FEP tube (0.8 mm I.D./1.2 mm O.D.) was attached to a syringe and the tube filled with methylcellulose. The methylcellulose was then removed from the tube so that only a thin coating remained on the tube wall.

Mounting of zebrafish embryos

The coated FEP tube was prepared for sample mounting by filling it with 0.1% agarose. Using a glass Pasteur pipette, a selected zebrafish embryo was transferred from the petri dish to the reaction tube containing 0.1% agarose at room temperature. Ideally, as little additional E3 as possible was transferred with the zebrafish to the reaction tube.

Using the syringe, the embryo was then pulled very gently into the tube towards the tip of the needle with its head first. Repeated pulling and pushing of the embryo was avoided. With a razor blade the tube was cut 1 to 2 mm above the head of the zebrafish embryo.

The FEP tube with the sample was then plugged with 3% low melting agarose. Before plugging the FEP tube, it was tipped slightly several times on the 3% low melting agarose dish so that only a minimal distance between head and plug remained after embedding. It was however avoided that the embryo touched the 3% melting agarose layer. The tube was placed straight on the 3% low melting agarose layer and turned slowly (like a screw) into the 3% plugging layer.

After embedding, the embryo was checked for integrity under the stereoscope.

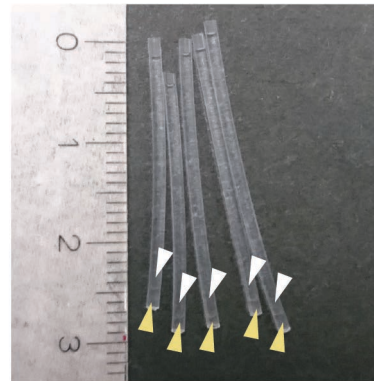


Fig. S2: Mounted single sample embryos

After mounting, zebrafish embryos (white arrowhead) rested on a 3% low melting agarose plug (yellow arrowhead)

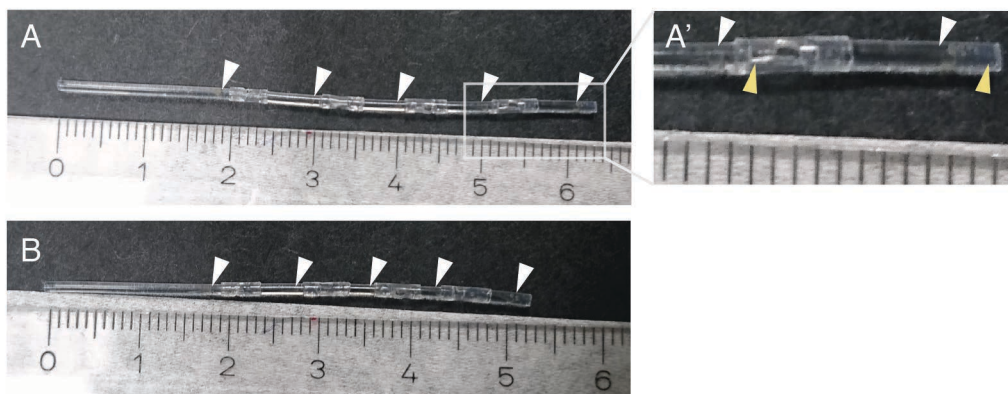


Fig. S3: Mounting of several embryos

Several embryos (white arrowheads) were mounted for an experiment. (A) The connectors were stacked so that the whole embryo was accessible. (A') Zoom in to A containing two fish (white arrowheads) and two plugs (yellow arrowheads). (B) only the head of the embedded fish was accessible resulting in a shorter overall tube.

3. Preparation of the multi-sample tube

The FEP tubes containing one mounted zebrafish embryo (Fig. S2) were cut to a length of about 9 mm providing space for the plug (about 2-3 mm), the zebrafish embryo (at the end of the time-lapse around 4 mm), and the connector (about 2-3 mm). The individual tubes were connected to form one long tube (Fig. S3). Depending on the experimental requirements, the overlap of the connector with the FEP tubes containing the sample could be varied. If only parts of the embryo such as the head were imaged, the tubes could be connected with a higher overlap, resulting in an overall shorter tube and the possibility to image more samples (Fig. S3, B). The hole in the tube not only increased oxygen availability in the sample tube but also made the procedure easier as no air pressure built up when connecting the tubes.

4. Potential embedding difficulties

Mounting of zebrafish embryos can be challenging. Below, some pitfalls and suggestions how to solve them are listed (Table S1)

Table S1: Suggestions for potential embedding problems

Problem	Solution
Dying embryos	<p>It is important that the embedding material is at room temperature before embedding. Zebrafish growth and survival is affected by too cold and too warm temperatures.</p> <p>After embedding, the integrity of the embryo should be checked under the stereomicroscope. Ideally, the embryo lies just above the plug but does not touch it yet.</p> <p>If dying samples reoccur, also changing the suppliers of any of the materials should be considered. Some people have reported that FEP tubes from some companies might be more likely to decrease sample health. The same applies for agarose. Also check for pH and possible contamination of E3. We only used filtered E3.</p>
Formation of air bubbles	<p>To avoid air bubbles, empty the syringe after sucking up the methylcellulose by disconnecting it from the cannula. Put the syringe and cannula back together, wipe the methylcellulose from the exterior of the FEP tube and rinse it several times with E3. Before mounting the embryo in the tube, also suck up some 0.1% agarose.</p> <p>Moreover, fill the dish containing the 3% low melting agarose to produce the plug with a bit of E3. This procedure reduces the formation of air bubbles during plugging.</p> <p>The 0.1% agarose might contain air bubbles. To remove them, vortex the reaction tube shortly before putting the fish into it.</p>
Zebrafish is far away from the plug after embedding	<p>Before plugging, tap the zebrafish several times on the 3% low melting agarose without plugging. This produces a suction force if the FEP tube is long enough. A length of 3.5 – 5 cm proved to be ideal for this.</p>
Zebrafish moves during imaging	<p>If you apply Tricaine as described in the original sample mounting paper (Kaufmann et al., 2012), zebrafish move at around 1 dpf. Therefore, we used alpha-bungarotoxin RNA in our long-term imaging studies. Also make sure that the embryo is close to the plug before starting an imaging experiment and that the FEP tubes have not been bent before the imaging was started.</p>

5. Material list

Table S2: List of Materials required for embedding

Name	Company / Catalog Number	Comments
Agarose, low melting temperature	Sigma / A9414	Supplied as powder
Bungarotoxin RNA		Stocks of 500 ng/ul were generated as described in (Swinburne et al., 2015)
Greiner Petri Dish	Sigma	Plastic, 94 mm x 16 mm and 60x15 mm
E3		Prepared as described in (Nüsslein-Volhard and Dahm, 2002), p. 22
Fluorinated Ethylene Propylene (FEP) tubes	Fluidflon FEP-Schlauch, Liquid Scan, pro liquid GmbH (http://www.proliquid.de) Art: 2001048_E	For the tube containing the growing zebrafish, an inner diameter (I.D.) of 0.8 mm and an outer diameter (O.D.) of 1.2 mm was chosen. The connectors were made of FEP tube with an I.D. of 1.1 mm and an O.D. of 1.5 mm.
Forceps	DUMONT / Dumostar Nr. 55 – Article 11295-51	Used for dechoriation of zebrafish embryos
Methylcellulose	Sigma / M0387	Supplied as powder
Omnifix-F Solo 1 ml Syringe	B. Braun Melsungen AG / 9161406V	
Phenol red solution	Sigma / P0290	For injection mix
Sterican Single-Use Cannula, blunt	B. Braun Melsungen AG Sterican 21G x 7/8" BD Blunt Fill Needle, 18G 1 1/2	For embedding, 0.8 mm x 22 mm cannula were used. To prepare the connectors, blunt ended needles (1.2 mm x 40 mm) were used.
Tricaine / MS-222	Sigma / E10521	Alternative mean of zebrafish immobilization instead of using bungarotoxin
70% EtOH		To clean the tube
1 M NaOH	Merck, 1091371000	To clean the tube
50 ml Polypropylene Centrifuge Tube	Corning / 430829	15 ml and 50 ml tubes were used as storage containers
1.5 ml reaction tube	Eppendorf / 3810X	

Adaptation of Fiji plugins to a SLURM cluster

1) To run the Fiji plugin on the cluster, add code so that macro input can be parsed on the cluster without running the GUI of FIJI.

```
import ij.IJ;
import ij.ImageJ;
import ij.Macro;
import ij.gui.GenericDialog;
import ij.plugin.PlugIn;

public class SPIM_yourplugin_ implements PlugIn {

    @Override
    public void run(String args) {

        //generate an object of GenericDialog class to which options can be
        //added and which can be evaluated
        final GenericDialog gd = new GenericDialog( "Indicate folder" );

        //generate options for the Plugin to work on SPIM data from the
        //multi-sample SPIM
        gd.addStringField( "Foldername ", "D:\\processfolder", 50 );
        gd.showDialog();

        if ( gd.wasCanceled() )
            return;

        // read in input from plugin interface
        String directory_name = gd.getNextString();

        // read in input if run as a plugin/macro on the cluster
        if(IJ.isMacro()){
            String options = Macro.getOptions();
            String[] listOptions = options.split(" ");
            String[] parsedOptions = new String[listOptions.length];
            IJ.log(options);
            for(int iter=0; iter<listOptions.length; iter++){
                String iterString = listOptions[iter];
                String[] tmpList = iterString.split("=");
                IJ.log(iterString);
                parsedOptions[iter] = tmpList[1];
            }
            directory_name = parsedOptions[0];
        }

        IJ.log(directory_name);
    }

    public static void main(String[] args2) {

        new ImageJ();
        IJ.runPlugIn("SPIM_yourplugin_ ", "");
    }
}
```


2) Install Fiji on the cluster, e.g. to the folder projects/yourproject/fiji

3) To launch the plugin on a cluster, here running with SLURM, it is convenient to prepare two files: (i) interface with SLURM (ii) interface with Fiji

(i) File to interface with slurm, e.g save as “start_yourplugin.sh”

```
#!/bin/bash
#SBATCH --nodes=1
#SBATCH --tasks-per-node=24
#SBATCH --cpus-per-task=1
#SBATCH --time=16:00:00
#SBATCH --mem 62000

/projects/yourproject/fiji/Fiji.app/ImageJ-linux64 --headless -macro
./run_yourplugin.ijm
```

Note: Here you specify parameters for the cluster, such as the number of nodes, tasks-per-node, CPUs per task, the time you estimate your plugin to run and the memory requirements for the tasks.

(ii) File to interface with Fiji, e.g. save as “run_yourplugin.ijm”

```
//set parameters for renaming and copy files
Foldername = "/projects/yourfolder";

//run it
run("SPIM_yourplugin_", "foldername =" +Foldername);
```

Note: The name of the plugin here "SPIM_yourplugin_" is the name specified in the scr/main/resources, plugins.config file.

(iv) now you can start your Fiji plugin from the command line:

```
sbatch start_yourplugin.sh
```

Note: If the .sh file is not found, be sure to be in the right folder where you also saved your .sh file

Growth characteristics of embedded zebrafish

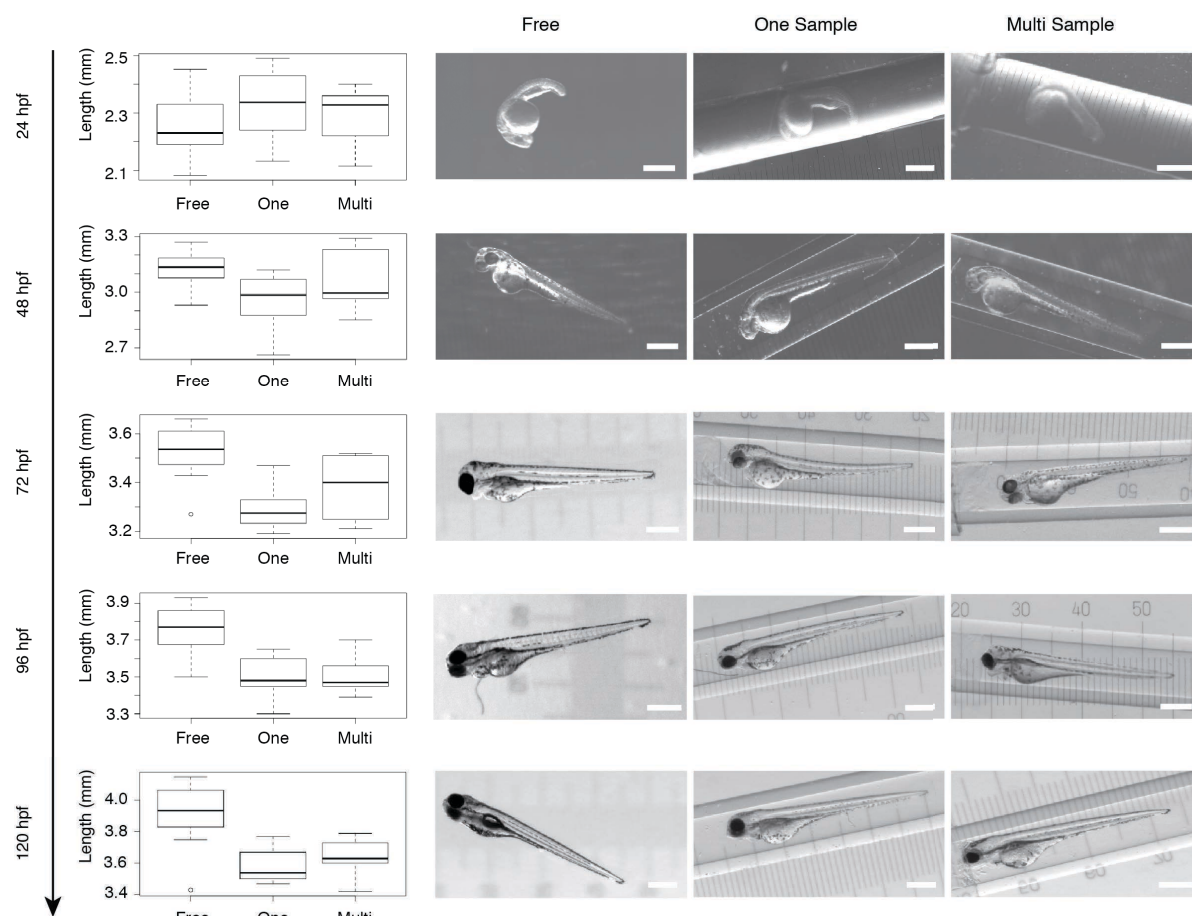
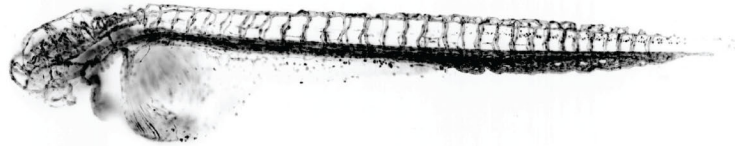


Fig. S4: Multi-sample embedding

Distribution of body length measurements of freely swimming fish ($n=8$), single embedded samples ($n=10$), and samples embedded in the multi-sample tube ($n=9$) with representative images for each embedding. The fish were embedded at 24 hpf. No morphological defects were observed with all three embedding protocols. Scale bar 500 μm .

Sample orientation for long-term imaging of the vasculature

- 60 degrees
from sagittal plane



dorsal detection
parallel to sagittal plane



+ 60 degrees
from sagittal plane

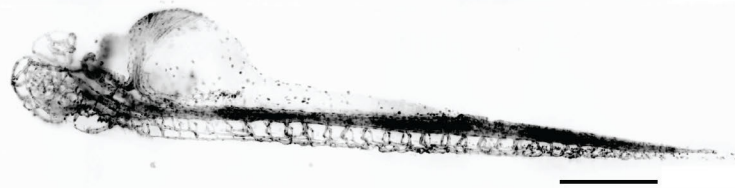


Fig. S5: Imaging directions of zebrafish.

Zebrafish embryos were imaged from three direction to have full access to the whole vasculature. Scale bar: 0.5 mm.

Automated data transfer

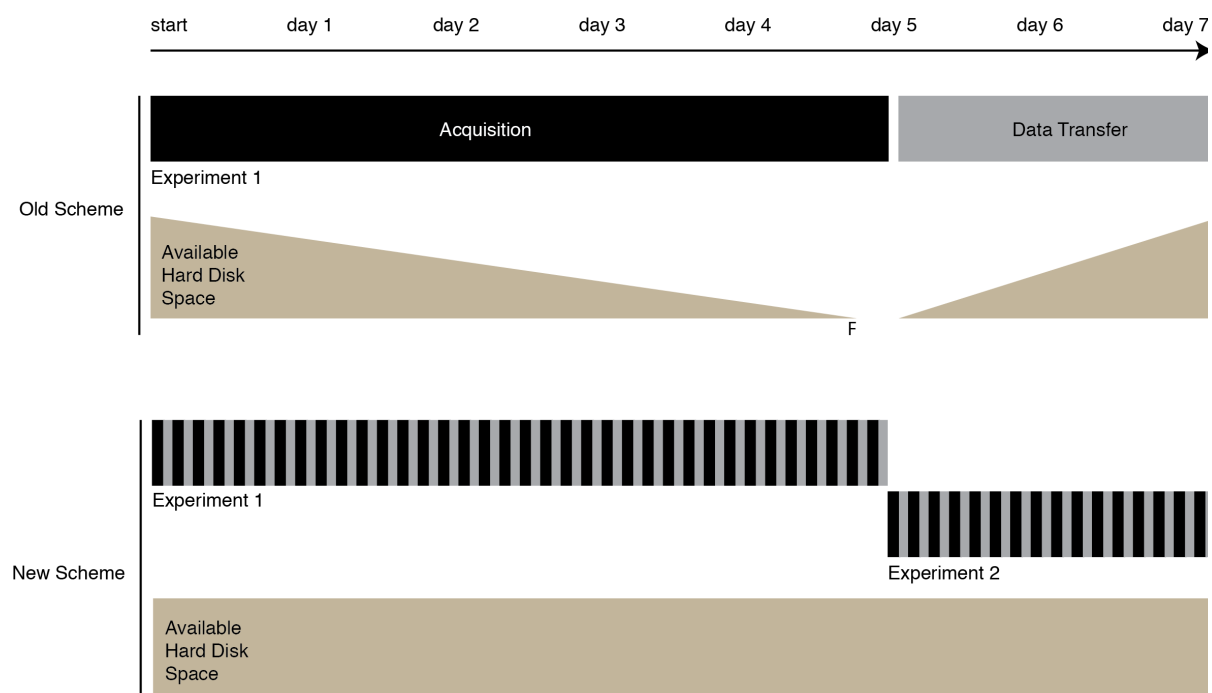


Fig. S6: Data transfer during acquisitions.

Comparison of old and new scheme. In the old scheme, data transfer (gray) did not start until data acquisition (black) was complete. With this acquisition scheme, there was a risk of filling the hard disks (F) before the end of the planned acquisition time. In the new scheme, after every acquisition (black), data is transferred (gray). Ideally, all data acquired was transferred, and therefore the available hard disk space did not decrease. Moreover, a new experiment could be started right at the end of first experiment leading to higher throughput.

Overview of processing pipeline

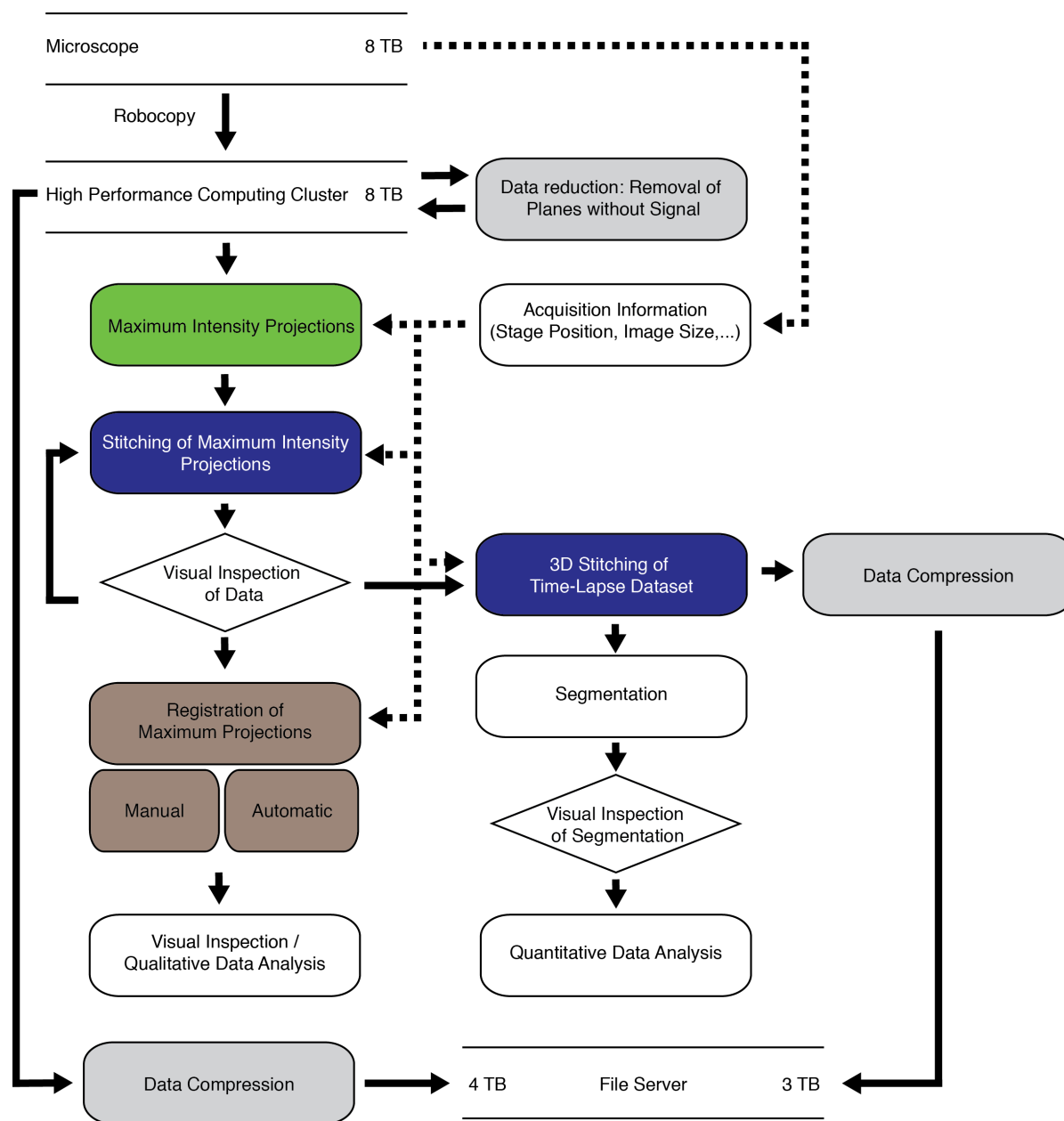


Fig. S7: Overview of data processing pipeline

The dedicated data processing pipeline was composed of modular parts for data compression (grey), projections (green), stitching of the data (blue), registration (brown), analysis (white). Full arrows indicated data flow, dashed arrow indicated the input of parameters from the microscope such as stage positions to the processing steps. Data quality was evaluated visually (\diamond) to ensure proper processing of the data.

Data stitching

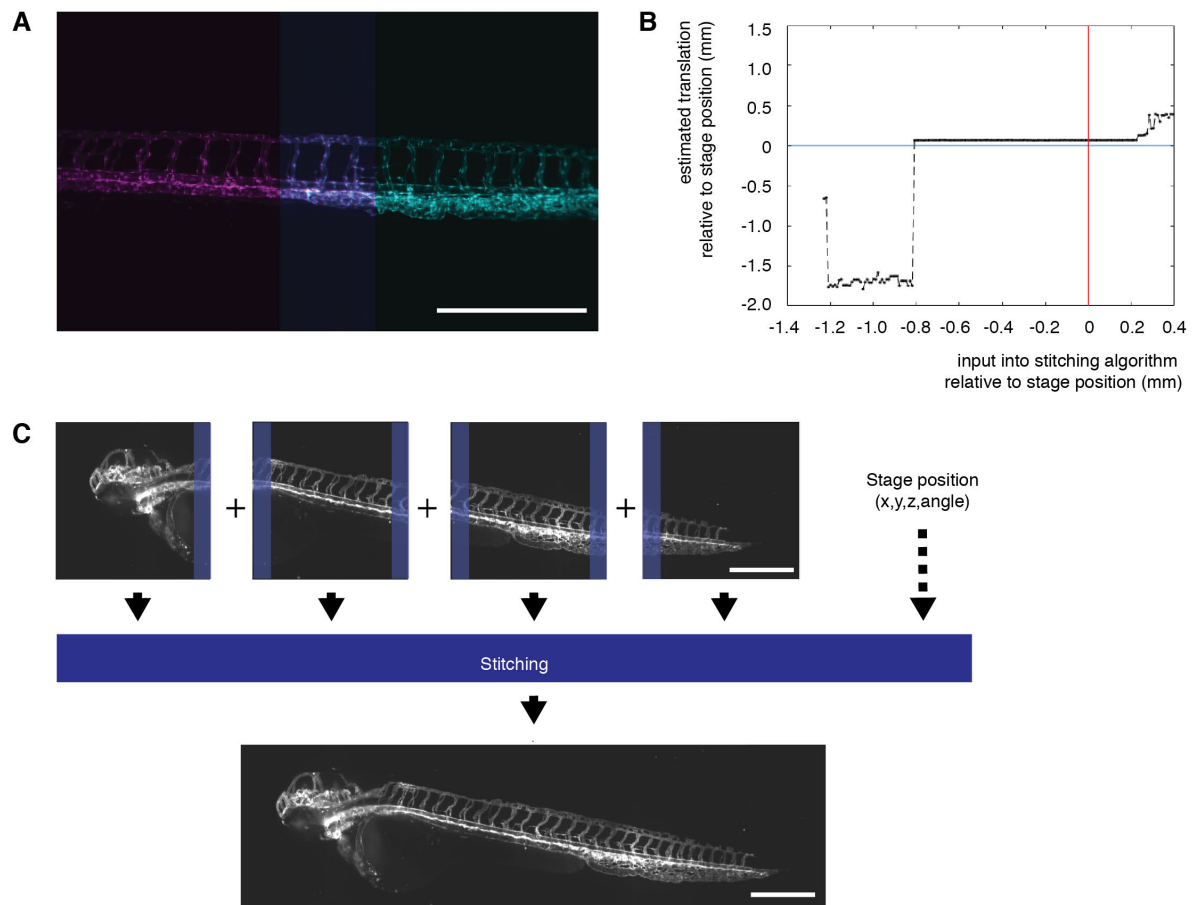


Fig. S8: Combining multiple acquisition volumes into one image: data stitching.

(A) Stitching of two images (magenta and cyan) zebrafish expressing the vascular marker Tg(kdrl:EGFP) (Jin et al., 2005). The overlap between the two images is highlighted in violet. (B) To automatically calculate the stitching of the two images in (A), an initial offset was set to initialize the calculation. Varying this offset revealed that it was robust over a large range of initialization values. Nevertheless, stitching became unreliable if the value were too far off from the assumed offset given by the translational stages (red line). Moreover, the stitching result indicated that the calculated translation (black line) was close to the physical coordinate given by the stage position (blue line) but not exact (0.06 mm / 53 pixels away). Therefore, using the stage position was a reasonable estimate for initialization. (C) In our implementation of stitching, stage positions determined which tiles to combine and then based on the initialization, the stitching generated a final output image. Here, a zebrafish expressing the vascular marker Tg(kdrl:Hsa.HRASmCherry) (Chi et al., 2008) is shown. Scale bar 0.5 mm.

Segmentation in different vascular regions

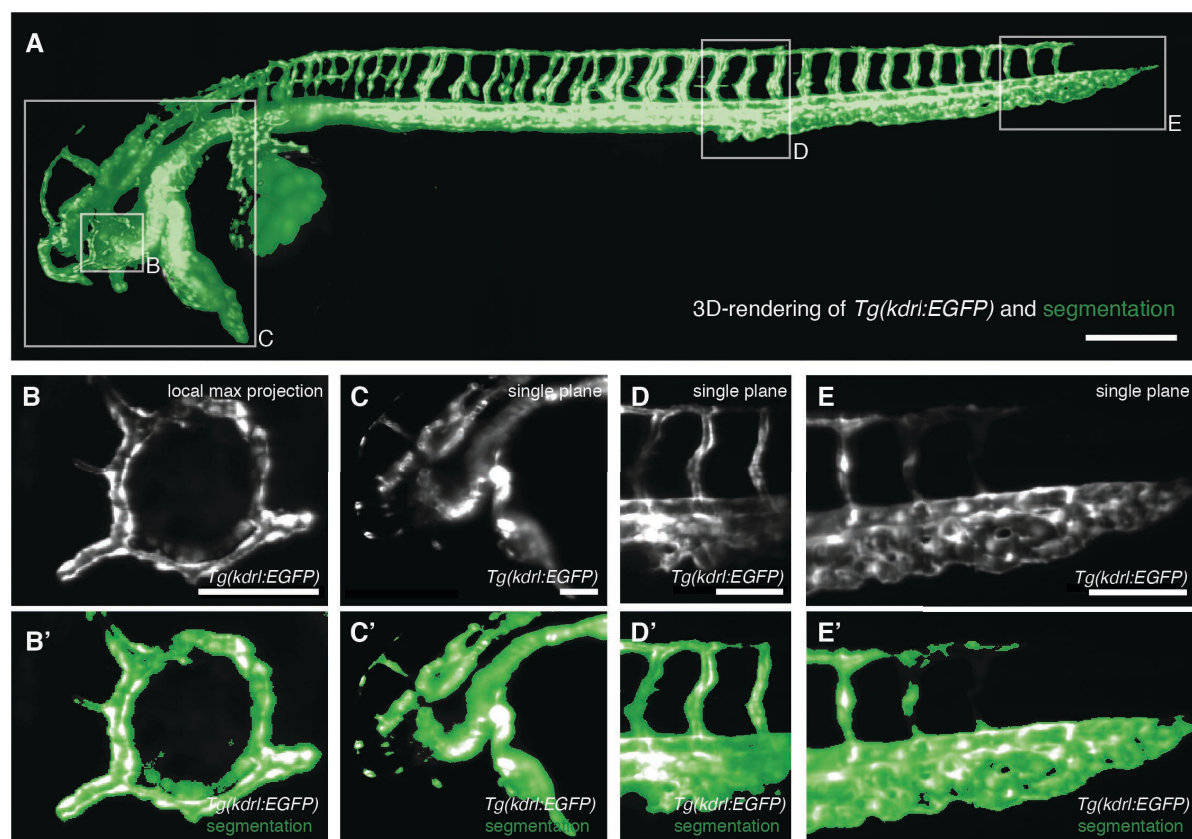


Fig. S9: Segmentation in different regions of the fish at around 2.5 dpf

(A) 3D rendering of the raw signal of the vascular marker *Tg(kdrl:EGFP)* (gray) overlaid with the segmentation obtained by our novel segmentation approach (green) with boxes depicting selected regions shown in (B-E, B'-E'). Scale bar: 0.25 mm. (B, B') Vascular marker (top) and overlay with segmentation (bottom) of a local maximum intensity projection over an 80 μ m deep 3D volume revealed the segmentation of the vasculature ring in the eye of zebrafish. Scale bar: 0.1 mm. (C, C') Vascular marker (top) and overlay with segmentation (bottom) of a single plane from a 3D volume revealed the segmentation quality in the head of the zebrafish. Scale bar: 0.1 mm. (D, D') Vascular marker (top) and overlay with segmentation (bottom) of a single plane from a 3D volume revealed segmentation quality in the tail of the zebrafish. Scale bar: 0.1 mm. (E, E') Vascular marker (top) and overlay with segmentation (bottom) of a single plane from a 3D volume revealed the segmentation quality at the end of the tail of the zebrafish. Scale bar: 0.1 mm.

Analysis and comparison of different growth models

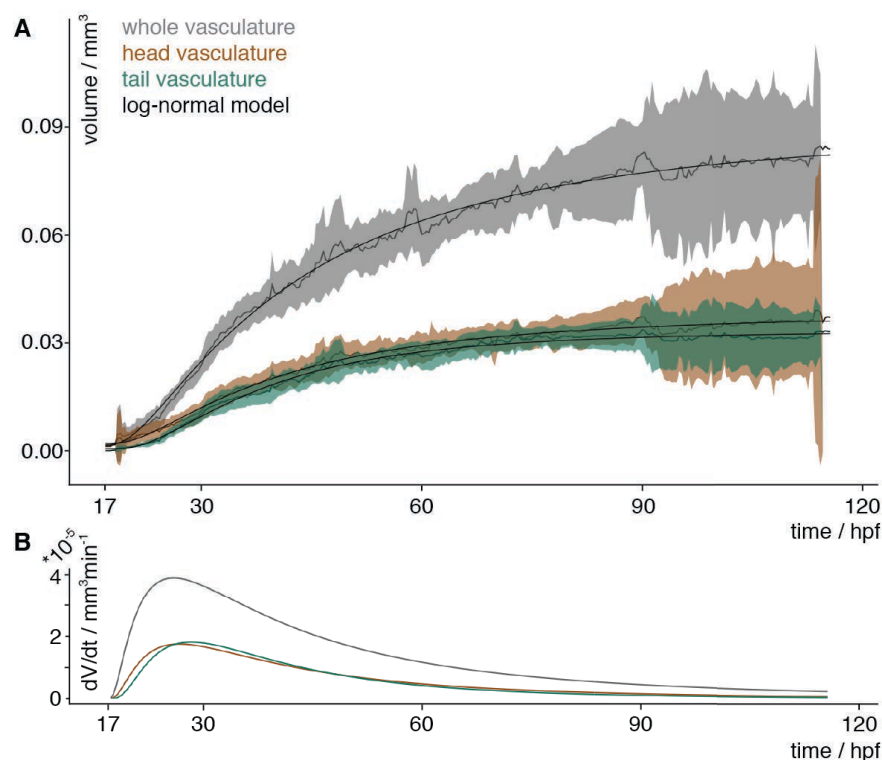


Fig. S10: Vascular volume growth characteristics of zebrafish described by the scaled cumulative log-normal growth model

(A) Experimental measurements of the volume over time of the whole vasculature (gray), the head (brown) and tail (turquoise) vasculature. The mean of the measurements is depicted with a solid line and the 95% confidence interval (t-statistics, $n=7$) as a ribbon in the corresponding color. The black line depicts the approximation of the volume by the scaled cumulative log-normal growth model.

(B) The volume growth rate of the whole vasculature (gray), head (brown) and tail (turquoise) was calculated by inserting the parameters obtained from the approximation into the change of volume equation from (Fig. 3B).

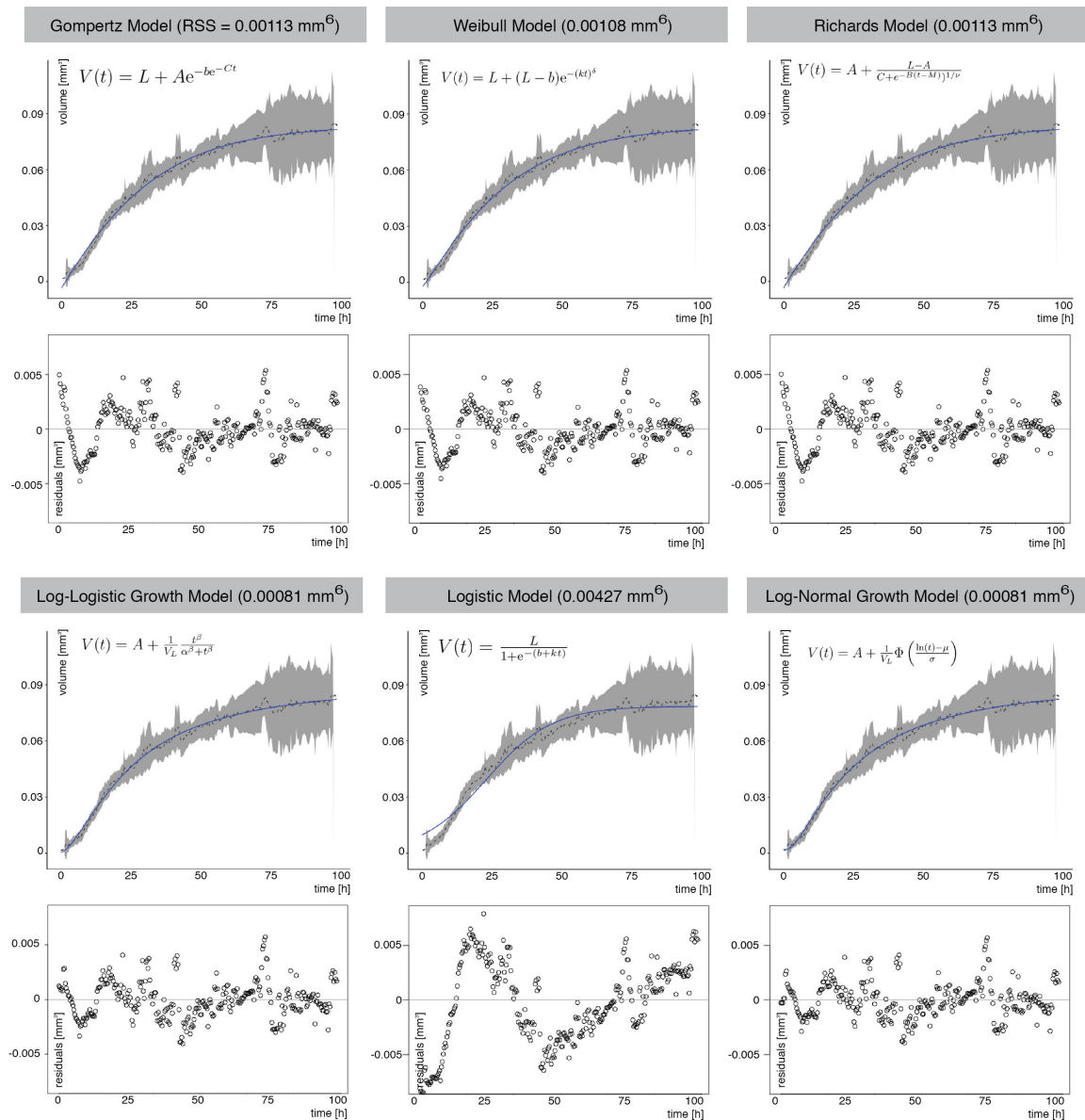


Fig. S11: Comparison of different growth models

The Gompertz model (Gompertz, 1825), Weibull model (Ratkowsky, 1983), Richards model (Richards, 1959; Tjørve and Tjørve, 2010), a normalized log-logistic growth model modified from (Bennett, 1983), the logistic model (Verhulst, 1938), and a normalized log-normal growth model modified from (Johnson et al., 1994) were compared and their residual sum of errors (RSS) calculated. A low RSS indicated a good fit. For each growth model, the predicted values from the model (blue line) were overlaid with the experimental data (dashed line – mean, gray ribbon 95% confidence interval). Moreover, for each growth model, the residuals were plotted over time. Small residual values combined with a random distribution of them around the 0 value (gray line) indicated good description of the data by the growth model. The log-normal and log-logistic growth models represented the data the best of all the tested models.

Development of the volume of the caudal vein plexus

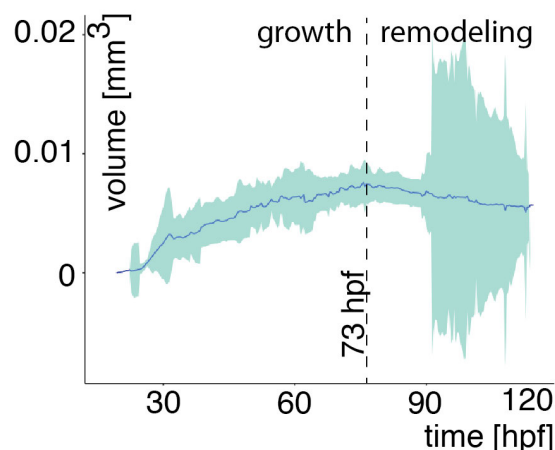


Fig. S12: Growth characteristics of the caudal vein plexus

The volume of the caudal vein plexus in the tail grew until around 73 hpf, after which its size started to decrease. The mean of the measurements is depicted with a blue line and the 95% confidence interval (t-statistics, $n=7$) as a ribbon in the light turquoise.

Phenotypic variation in zebrafish vasculature

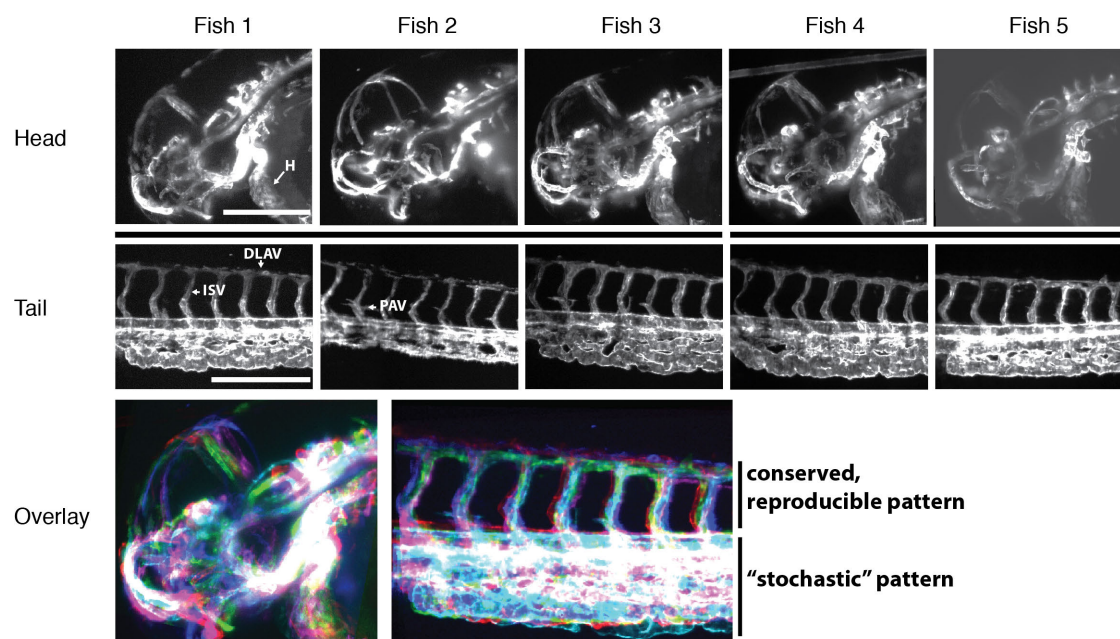


Fig. S13: Phenotypic variation of zebrafish vasculature

Five zebrafish expressing the vasculature marker *Tg(kdr:lfeactGFP)* (Vanhollebeke et al., 2015) at 35 hpf were imaged using SPIM. Maximum projections of the head and tail of five different individual zebrafish embryos (H, heart; DLAV, dorsal longitudinal anastomotic vessel; ISV, intersegmental vessels; PAV, parachordal vessel). Scale bar: 0.25 mm. Overlay of the head and the tail parts revealed different degrees of variation in the vasculature. The bright white signal indicates maximum overlap.

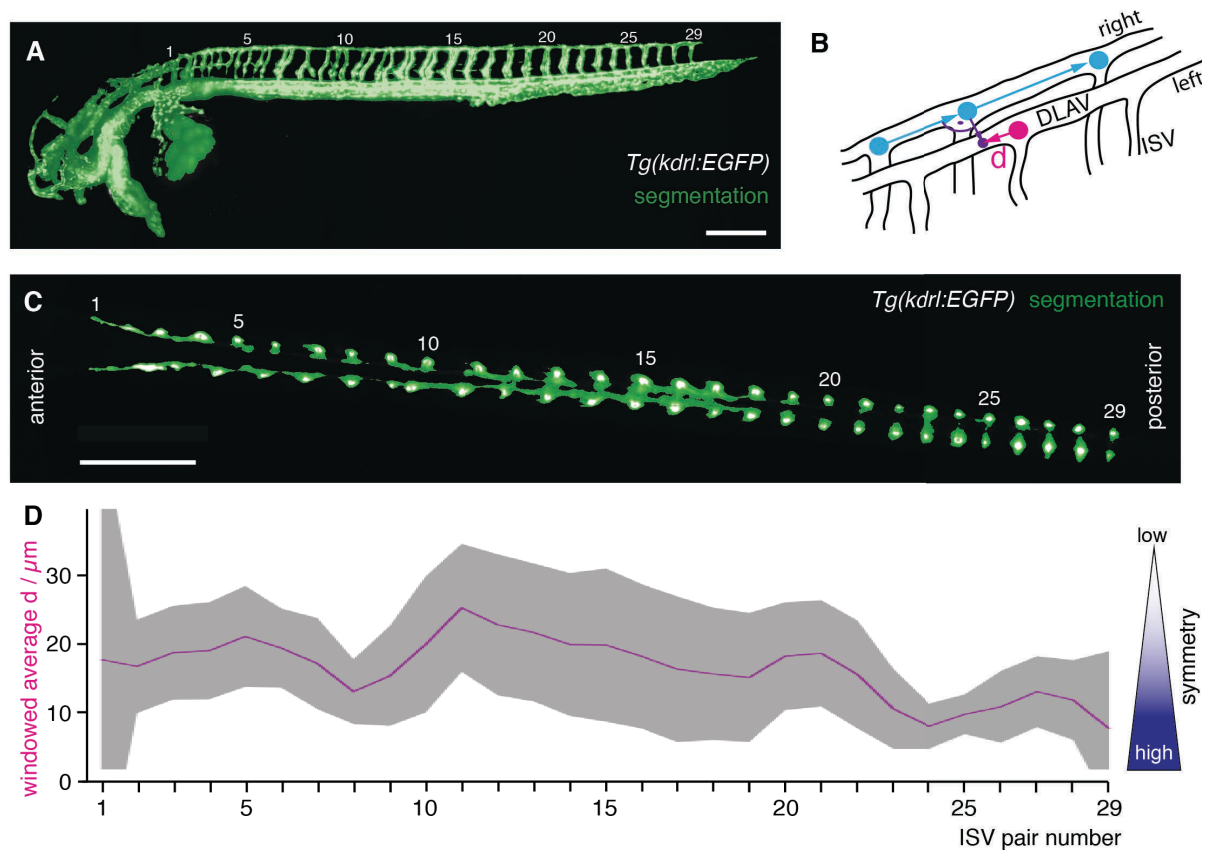
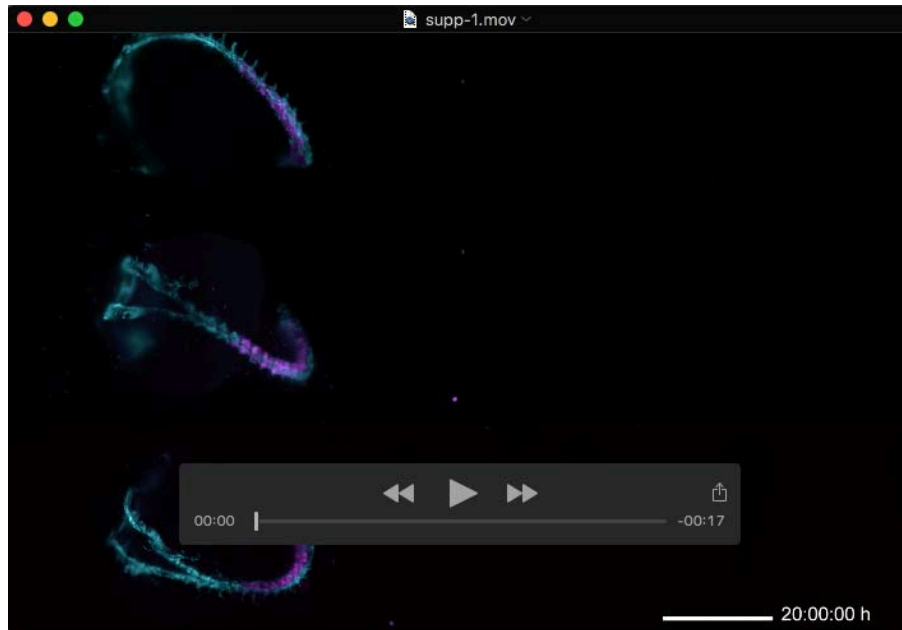


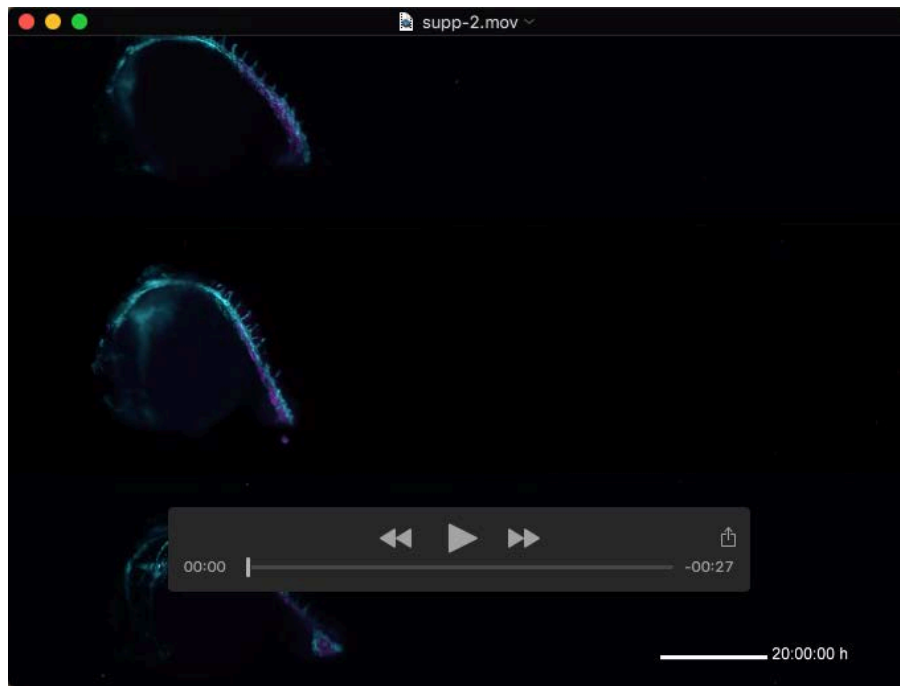
Fig. S14: Quantification of symmetry of intersegmental vessel (ISV) pairs along the anterior-posterior axis at around 2.5 dpf

(A) 3D rendering of the raw signal of the vascular marker *Tg(kdrl:EGFP)* (gray) overlaid with the segmentation obtained by our novel segmentation approach (green). The ISV pairs along the anterior-posterior axis were numbered (1-29). Scale bar: 0.25 mm. **(B)** Schematic of the quantification of symmetry of ISV pairs. For each ISV of the right side (cyan circles), the corresponding closest ISV of the left side (magenta circle) was determined. The symmetry was measured as absolute value of the distance *d* of the intersection (purple circle) with the ISV position of the closest left ISV (magenta circle). The intersection (purple circle) was calculated as point where the vector of direction of the DLAV of the left side (magenta vector) with the vector originating at the right ISV position with an angle of 90 degrees to the right DLAV (purple vector) met. **(C)** Single slice from 3D stack imaged from the dorsal direction revealed the arrangement of the ISVs pairs numbered from 1-29. In this slice, the raw signal of the vascular marker *Tg(kdrl:EGFP)* (gray) was overlaid with the segmentation (green). Scale bar: 0.25 mm. **(D)** Result of the quantification of symmetry *d* from 3 fish. To decrease noise in the calculation, the value of the distance *d* was indicated as windowed average over the neighboring ISV pairs, i.e. *n*=9 (3 fish and 3 ISV pairs/data point) except for the ISV pair 1 and 29 where *n*=6 (3 fish, 2 ISV pairs). The average value was indicated as solid magenta line with the 95% confidence interval (t-statistics, *n*=9 [ISV pair 2-28], *n*=6 [ISV pair 1 and 29]) as a ribbon in gray.



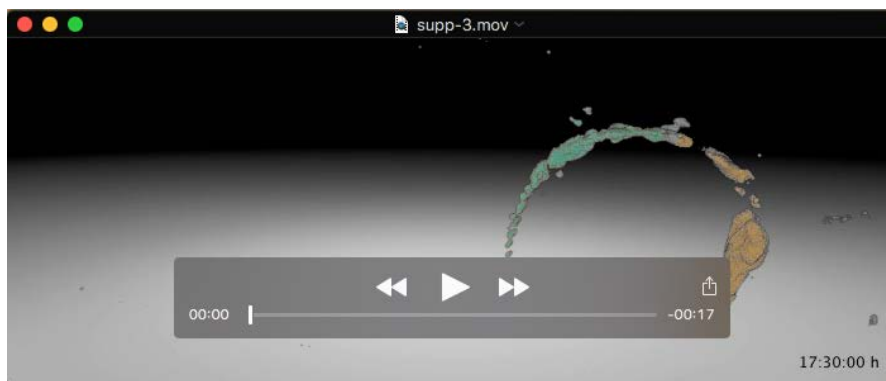
Movie 1

Zebrafish embryos expressing the fluorescent vascular marker *Tg(kdrl:EGFP)* in cyan and the red blood cell marker, *Tg(GATA1a:dsRed)* in magenta imaged from three different angles over several days. Scale bar: 0.5 mm.



Movie 2

Three different zebrafish embryos expressing the fluorescent vascular marker *Tg(kdrl:EGFP)* in cyan and the red blood cell marker, *Tg(GATA1α:dsRed)* in magenta imaged in the same experiment simultaneously over several days. Scale bar: 0.5 mm.



Movie 3

3D-rendered segmentation of the zebrafish vasculature with annotations of the head vasculature in orange, the tail in turquoise with its caudal vein plexus highlighted with light-turquoise and unannotated vasculature in grey.

References

- Bennett, S.** (1983). Log-Logistic Regression Models for Survival Data. *Journal of the Royal Statistical Society. Series C (Applied Statistics)* **32**, 165–171.
- Chi, N. C., Shaw, R. M., De Val, S., Kang, G., Jan, L. Y., Black, B. L. and Stainier, D. Y. R.** (2008). Foxn4 directly regulates tbx2b expression and atrioventricular canal formation. *Genes Dev* **22**, 734–739.
- Gompertz, B.** (1825). On the nature of the function expressive of the law of human mortality, and on a new mode of determining the value of life contingencies. *Philos Trans R Soc Lond B Biol Sci* 513–585.
- Jin, S.-W., Beis, D., Mitchell, T., Chen, J.-N. and Stainier, D. Y. R.** (2005). Cellular and molecular analyses of vascular tube and lumen formation in zebrafish. *Development* **132**, 5199–5209.
- Johnson, N. L., Kotz, S. and Balakrishnan, N.** (1994). *Continuous univariate distributions*. John Wiley & Sons, Inc.
- Kaufmann, A., Mickoleit, M., Weber, M. and Huisken, J.** (2012). Multilayer mounting enables long-term imaging of zebrafish development in a light sheet microscope. *Development* **139**, 3242–3247.
- Nüsslein-Volhard, C. and Dahm, R.** (2002). *Zebrafish: A Practical Approach*. Oxford University Press.
- Ratkowsky, D. A.** (1983). *Nonlinear Regression Modeling*. Dekker.
- Richards, F. J.** (1959). A Flexible Growth Function for Empirical Use. *Journal of Experimental Botany* **10**, 290–301.
- Swinburne, I. A., Mosaliganti, K. R., Green, A. A. and Megason, S. G.** (2015). Improved Long-Term Imaging of Embryos with Genetically Encoded α -Bungarotoxin. *PLoS ONE* **10**, e0134005.
- Tjörve, E. and Tjörve, K. M. C.** (2010). A unified approach to the Richards-model family for use in growth analyses: Why we need only two model forms. *Journal of Theoretical Biology* **267**, 417–425.
- Vanhollebeke, B., Stone, O. A., Bostaille, N., Cho, C., Zhou, Y., Maquet, E., Gauquier, A., Cabochette, P., Fukuhara, S., Mochizuki, N., et al.** (2015). Tip cell-specific requirement for an atypical Gpr124- and Reck-dependent Wnt/ β -catenin pathway during brain angiogenesis. *Elife* **4**, 2807.
- Verhulst, P. F.** (1938). Notice sur la loi que la population suit dans son accroissement. *Correspondance mathématique et physique* 113–121.
- Weber, M., Mickoleit, M. and Huisken, J.** (2014). Multilayer Mounting for Long-term Light Sheet Microscopy of Zebrafish. *J. Vis. Exp.* e51119–e51119.
- Westerfield, M.** (2000). *The zebrafish book. A guide for the laboratory use of zebrafish Danio rerio*. 4 ed. Eugene: Univ. of Oregon Press.
- White, R. M., Sessa, A., Burke, C., Bowman, T., LeBlanc, J., Ceol, C., Bourque, C., Dovey, M., Goessling, W., Burns, C. E., et al.** (2008). Transparent adult zebrafish as a tool for in vivo transplantation analysis. *Cell Stem Cell* **2**, 183–189.